Heron Eduardo de Lima Ávila

Analysis and development of a resonant frequency tracking system for a resonant cavity sensor

Tese submetida ao Programa de Pós-graduação em Engenharia Elétrica da Universidade Federal de Santa Catarina para a obtenção do Grau de Doutor em Engenharia Elétrica
Orientador: Prof. Dr. Fernando Rangel de Sousa
Coorientador: Prof. Dr. Daniel Juan Pagano

Florianópolis
2018

Ficha de identificação da obra elaborada pelo autor,
através do Programa de Geração Automática da Biblioteca Universitária da UFSC.

Ávila, Heron Eduardo de Lima
Analysis and development of a resonant frequency tracking system for a resonant cavity sensor / Heron Eduardo de Lima Ávila ; orientador, Fernando Rangel de Sousa, coorientador, Daniel Juan Pagano, 2018.
132 p.

Tese (doutorado) - Universidade Federal de Santa Catarina, Centro Tecnológico, Programa de Pós Graduação em Engenharia Elétrica, Florianópolis, 2018.

Inclui referências.

1. Engenharia Elétrica. 2. Engenharia Elétrica. 3. Instrumentação industrial. 4. Sensor ressonante. 5. Circuito PLL. I. de Sousa, Fernando Rangel. II. Pagano, Daniel Juan. III. Universidade Federal de Santa Catarina. Programa de Pós-Graduação em Engenharia Elétrica. IV. Título.

Heron Eduardo de Lima Ávila

ANALYSIS AND DEVELOPMENT OF A RESONANT FREQUENCY TRACKING SYSTEM FOR A RESONANT CAVITY SENSOR

Esta Tese foi julgada adequada para obtenção do Título de Doutor em Engenharia Elétrica e aprovada em sua forma final pelo Programa de Pós-Graduação em Engenharia Elétrica da Universidade Federal de Santa Catarina.

Florianópolis, 15 de Outubro de 2018.

_____
Prof. Bartolomeu Ferreira Uchôa Filho, Dr.
Coordenador do Curso

_____
Prof. Fernando Rangel de Sousa, Dr.
Orientador
Universidade Federal de Santa Catarina

_____
Prof. Daniel Juan Pagano, Dr.
Coorientador
Universidade Federal de Santa Catarina

Banca Examinadora:

_____
Prof. Sebastian Yuri Catunda, Dr.
Universidade Federal do Rio Grande do Norte

_____
Prof. Francisco Rafael Moreira da Mota, Dr.
Instituto Federal de Santa Catarina

_____
Prof. Paulo Márcio Moreira e Silva, Dr.
Instituto Federal de Santa Catarina

Aos meus pais Joel e Lizmara, à minha irmã Paula (quem me alfabetizou) e à minha adorável sobrinha Sarah, dedico.

AGRADECIMENTOS

Agradeço a todas as mentes brilhantes que ao longo da evolução da humanidade desenvolveram o conhecimento que tornou possível a implementação deste trabalho.

Aos órgãos de fomento à pesquisa que ao longo de minha formação acadêmica me proveram suporte financeiro, pontualmente ao CNPq nesta etapa de doutoramento, e também ao apoio logístico e administrativo recebido da Universidade Federal de Santa Catarina.

Expresso meu agradecimento ao prof. Fernando Rangel de Sousa pela sua orientação e apoio, tanto no aspecto técnico e profissional, quanto em questões pessoais. Agradeço também ao prof. Daniel Juan Pagano pela sua participação e aceite para coorientar esta pesquisa. Meus agradecimentos também se estendem aos demais professores que de alguma maneira colaboraram para a revisão e melhoria do trabalho.

Registro, também, meu sincero agradecimento aos colegas do LRF, pela parceria e apoio que muito enriqueceram não só meu conhecimento técnico-científico, mas também minha formação social.

Desejo, finalmente, mas não menos importante, agradecer aos meus pais, minha irmã e demais familiares e amigos pelo incentivo e suporte ao longo desses anos.

LIST OF SYMBOLS

E Electric field

B Magnetic field

c Speed of the wave propagation

c_o Speed of the light in vacuum

μ Permeability of the medium

ε Permittivity of the medium

f_r Resonant frequency

a Cavity radius

d Cavity length

Q Quality factor

Q_u Unloaded quality factor

Q_l Loaded quality factor

Q_e External quality factor

IL Insertion Loss

ϕ Phase shift

Z_s Source impedance

Z_L Load impedance

C Variable capacitance

L Inductance

k Constant regarding the geometry of the sensor

R_1, R_2 Resistances representing the losses in the sensor

u_{rcs} RCS's input signal

y_{rcs} RCS's output signal

u_{pd} Reference input signal of the phase detector

ϕ_r Phase reference

φ_e Phase error

φ System phase shift

y_c Control signal

$\Delta\phi_{rcs}$ Phase shift of the RCS path

$\Delta\phi_{pd}$ Phase shift of the PD path

φ_{vco} VCO phase

ω_{vco} VCO oscilating frequency

ω_c VCO center oscilating frequency

K_{vco} VCO gain

φ_{rcs} RCS total phase shift

$\Delta\varphi$ RCS phase dynamic

$\hat{y}_{rcs}$ RCS amplitude dynamic

y_{pdi} In-phase PD signal

y_{pdq} Quadrature PD signal

$\Delta\phi_q$ Phase shift of the quadrature path

$\Delta\phi_i$ Phase shift of the in-phase path

ω_g Low-pass filter Cut-off frequency

W_f Water fraction

RESUMO

O monitoramento e controle em linha de aplicações industriais são de fundamental importância para garantir a segurança e a credibilidade dos processos de fabricação. A garantia da qualidade depende da confiabilidade dos sensores e instrumentos empregados. Sensores ressonantes têm sido estudados desde a década de 1950, uma vez que seu princípio de funcionamento permite a medição de diferentes grandezas físicas. Um tipo específico de ressonador baseado em cavidades ressonantes tem sido largamente empregado em diversas aplicações, como relatado na literatura. Esta tese está relacionada com a análise e avaliação de um sensor de cavidade ressonante como parte de um sistema de medição com potencial para melhorar as capacidades de monitoramento de sensoriamento em linha em setores distintos da indústria. Duas aplicações industriais são consideradas, sendo a primeira envolvendo a detecção da fração de água em fluxos gás-líquido, na indústria de petróleo e gás, e a segunda envolvendo a detecção de sólidos totais e teor de gordura na indústria de laticínios. Para estas aplicações, foi desenvolvido um sistema de rastreamento da freqüência de ressonância, baseado em uma técnica de malha travada em fase (*Phase-locked loop - PLL*), considerando toda a modelagem do sistema, análise experimental e validação. Além disso, um sistema automático para o processo de padronização do leite em plantas laticinistas, que é uma das etapas mais importantes na produção do leite, também é proposto.

Palavras-chave: sensor de cavidade ressonante, sistema de rastreamento da frequência de ressonância, medição de fração de água, medição de gordura no leite, PLL.

RESUMO EXPANDIDO

Introdução

O fenômeno da ressonância está presente na natureza de diversas formas. Entendê-lo tornou possível à humanidade construir desde um simples balanço para crianças até complexos sistemas de telecomunicações.

Estruturas ressonantes são caracterizadas pela presença de uma frequência natural de oscilação. Em ressonadores mecânicos, por exemplo, a frequência natural ou frequência de ressonância é determinada por suas características mecânicas como módulo de elasticidade, massa e estrutura física. Ao oscilar, a energia se alterna entre energia cinética e potencial. Em ressonadores elétricos, como os circuitos LC, as energias armazenadas alternam entre energia magnética (armazenada no campo magnético do indutor) e energia elétrica (armazenada no campo elétrico do capacitor).

Sensores baseados em estruturas ressonantes são frequentemente utilizados em inúmeros sistemas de medição para inferir diferentes tipos de grandezas físicas, tais como massa, deslocamento, força, temperatura, permissividade, além de propriedades químicas dos materiais como densidade e viscosidade.

Levando esses requisitos em consideração, esta pesquisa centrou a sua atenção em um sensor ressonante baseado na tecnologia de cavidades ressonantes. As cavidades ressonantes podem ser consideradas como seguimentos de guias de onda que apresentam formas retangulares ou cilíndricas. A estrutura pode ser curto-circuitada nas extremidades com paredes metálicas, como em sensores utilizados em laboratório para medir amostras isoladas de determinados materiais, ou ainda aberta em ambas as extremidades para permitir o fluxo do material. Esta última abordagem foi o foco da pesquisa que avaliou a utilização deste sensor em duas aplicações distintas na indústria de petróleo e laticinista.

Para tanto, buscou-se a implementação de um sistema de rastreamento da frequência de ressonância a partir de uma técnica de malha travada em fase (conhecida como PLL do inglês *Phase-locked-loop*), comumente utilizada em sistemas de telecomunicações.

A utilização deste sensor, quando inserido em um sistema de rastreamento da frequência de ressonância a partir de uma tecnica PLL, fornece um sistema de medição autônomo completo que pode ser empregado para medições em linha como solução viável em diferentes aplicações industrais.

Objetivos

Neste trabalho de pesquisa, buscou-se contribuir na área de técnicas de medições para sensores ressonantes, especificamente para sensores baseados na tecnologia de cavidades ressonantes empregados em aplicações industriais para o monitoramento em linha de diferentes grandezas físicas.

Duas aplicações distintas foram investigadas, sendo (i) determinação da fração de água em escoamentos estratificados de duas fases (água/gás), empregado na indústria de petróleo e (ii) determinação do percentual de gordura no leite, empregado na indústria laticinista.

Os objetivos específicos do trabalho são:

1. Identificar o modelo matemático do sensor e melhorar a confiabilidade das medições através da análise de adaptação de impedâncias;

2. Elaborar uma técnica de rastreamento da frequência de ressonância para, em conjunto com o sensor, fornecer um sistema de medição autônomo completo;

3. Modelar o sistema de forma rigorosa levando em conta as não linearidades das dinâmicas envolvidas e prover um modelo completo para a análise e elaboração de técnicas avançadas de controle;

4. Comprovar a viabilidade do emprego do sistema nas duas aplicações estudadas.

5. Gerar uma base consistente para a continuidade de pesquisas mais avançadas nesta mesma temática que permitam o estudo, por exemplo, de novas correlações entre os parâmetros de medição do sistema e as grandezas físicas de interesse.

Metodologia

Para atingir os objetivos propostos, foram realizados os procedimentos listados a seguir:

1. Estudo das técnicas de adaptação de impedâncias aplicadas para adaptar cargas complexas à impedância de circuitos projetados para 50 Ω;

2. Análise e modelagem matemática do sensor de cavidade ressonante com validação experimental;

3. Análise e modelagem matemática do sistema de medição empregando uma técnica baseada em PLL para o rastremaento da frequência de ressonância;

4. Análise e projeto do controlador empregando técnicas clássicas de controle no sistema linearizado e validação experimental;

5. Validação experimental das aplicações industriais abordadas.

Resultados e Discussão

A contribuição geral desta Tese está relacionada à exploração de técnicas de medição para o rastreamento em tempo real da frequência de ressonância de um sensor de cavidade ressonante, que é apropriado para medições de processos industriais em linha. As contribuições específicas são listadas abaixo:

- A respeito do sensor, foram projetadas redes de adaptação para o aumento da transferência de potência do sinal e consequente melhoria da confiabilidade das medições;

- Foi proposto um modelo elétrico, a partir de um circuito ressonante clássico RLC, para investigar a dinâmica do sensor utilizando ferramentas de análise em frequência e temporal;

- Foi desenvolvido um modelo semi-empírico do sistema de rastreamento da frequência de ressonância, a partir de uma técnica baseada em um circuito PLL. A modelagem foi feita sob uma perspectiva matemática rigorosa levando em conta as não idealidades dos componentes, o que resultou em um sistema autônomo não linear de oito estados para análie em malha fechada. A validação experimental demonstrou a viabilidade da utilização de técnicas de controle clássico levando em conta o sistema linearizado em torno da frequência de ressonância;

- Considerando as aplicações investigadas, no monitoramento da fração de água em um padrão de escoamento com variação laminar do conteúdo de água, o sensor foi capaz de inferir a fração de água em toda a faixa entre 0% e 100% de fração de água com uma sensibilidade média relativa de 0,17% por fração de água. Na determinação do conteúdo de gordura e de total de sólidos no leite bovino, foi detectada uma alta correlação e uma dependência linear entre a frequência de ressonância do sensor e o percentual de gordura e total de sólidos do leite;

- A utilização do sensor de cavidade ressonante inserido em um sistema de rastreamento da frequência de ressonância, utilizando uma técnica de medição baseada em um circuito PLL, pode ser considerada uma contribuição legítima da Tese (até aonde a pesquisa pode confirmar);
- Por fim, a proposta de um sistema para o controle automático do processo de padronização do leite, também contribui de forma legítima para a solução de um problema latente na indústria laticinista nacional, que apresenta várias lacunas para a implementação de tecnologias que possam melhorar a qualidade dos produtos nacionais, além de otimizar os diferentes processos envolvidos na etapa de beneficiamento e produção do leite e seus derivados.

Considerações Finais

Os objetivos traçados no começo da pesquisa foram atingidos, contribuindo assim para o projeto de sistemas aplicados ao monitoramento de diferentes grandezas físicas em linha nos processos industriais, por meio do rastreamento da frequência de ressonância de sensores baseados na tecnologia de cavidades ressonantes. Os resultados obtidos poderão servir de base para futuros trabalhos, os quais podem incluir, por exemplo, a análise não linear do sistema para a definição teórica e experimental dos intervalos de interesse do PLL (*Pull-in, Lock-in, Hold-in*), além do estudo de possíveis correlações entre as informações de magnitude e frequência de ressonância com parâmetros de interesse do sistema em análise.

Palavras-chave: sensor de cavidade ressonante, sistema de rastreamento da frequência de ressonância, medição de fração de água, medição de gordura no leite, PLL.

ABSTRACT

The in-line monitoring and control of industrial applications are of fundamental importance to guarantee the safety and fidelity of the manufacturing processes. The assurance of quality depends on the reliability of the sensors and instruments employed. Resonant sensors have been studied since the decade of 1950s, since their working principle allows the measurement of different physical quantities. A specific type of resonator, the so called resonant cavity resonator, has achieved great interest, and researches, regarding its usage in several applications, have been published. This thesis is concerned with the analysis and evaluation of a resonant cavity sensor as part of a measurement system with potential to improve the capabilities of in-line sensing monitoring in distinct industry sectors. Two industrial applications are considered: the detection of water fraction in gas-liquid flows, in oil and gas industry, and the detection of total solids and fat contents in dairy industry. For these applications, we present a resonant frequency tracking system, based on a phase-locked loop technique, including for the whole system modeling, experimental analysis and validation. Furthermore, we explore a project regarding the standardization process in dairy facilities, which is one of the most important stage in milk production.

Keywords: resonant cavity sensor, resonant frequency tracking system, water fraction measurement, milk fat measurement, PLL.

LIST OF FIGURES

LIST OF TABLES

CONTENTS

1 INTRODUCTION

1.1 BACKGROUND AND MOTIVATION

The resonance phenomenon is present in nature in an intrinsic way. Understanding its behavior enabled mankind to build from a simple swing for children to a complex telecommunication system.

Resonant structures are characterized by the presence of a natural oscillation frequency. In mechanical resonators, for example, the natural frequency or resonant frequency is determined by its mechanical characteristics, such as modulus of elasticity, mass and physical structure. By oscillating, energy alternates between kinetic and potential energies [1]. In electrical resonators, such as LC circuits, the stored energies alternate between magnetic energy (stored in the inductor's magnetic field) and electrical energy (stored in the capacitor's electric field).

Sensors based on resonant structures are often used in several measurement systems to infer different types of physical quantities, such as mass [2], displacement [3], [4], force [5], temperature [6], permittivity [7], physical properties of materials, for instance, density and viscosity, [8], [9].

The operating principle of the resonant sensors is based on the relationship between its resonant frequency and the physical quantity to be measured. There are also micro-electromechanical (MEMS) and nano-electromechanical (NEMS) resonant systems which, with the improvement of microelectronics, have become quite popular in several applications [10], [11].

Another way to infer a given measurand is by indirect measuring a physical quantity and relating it to the desired variable. As an example, we can mention the measurement of water fraction in multiphase flows using a Resonant Cavity Sensor (RCS) [12], [13], [14]. In this scenario, the RCS's resonant frequency varies according to the effective permittivity of the flow pattern. The permittivity in turn, varies as a consequence of the water fraction.

Resonant cavities can be considered as short segments of waveguides that have rectangular or cylindrical shapes. The structure can be short-circuited at the ends with metal walls, such as sensors used in laboratory to measure samples isolated from certain materials, or open at both ends to allow the flow of the material, as in industrial

sensors employed in multiphase flow measurement systems in oil and gas industry [15], and for monitoring the milk constituents in dairy industry [16].

Multiphase flow measurement is a fairly common problem in the oil and gas industry, where multiphase flows composed of salt water, gas, oil and sand are present at various stages of oil production. The most common classes are the two phase flows, which may include gas-solid flow, where solid particles are suspended in gases; liquid-liquid emulsions, which include oil and water emulsion flow in pipes; liquid-solid, which are widely found in hydraulic transmissions of solid material, and gas-liquid, that is probably the most important form of multiphase flow being widely found in various industrial applications.

In other sectors, as in the food industry, there is a constant concern about the quality of the industrialized products and the optimization of the manufacturing processes. Specifically, in dairy industry, the monitoring of milk quality is mandatory for satisfying standards and regulations, besides avoiding any type of fraud that can put the consumer's health at stake risk.

According to the last report of the U.S. Energy Information Administration (EIA) [17], since 2014 Brazil went back to the top 10 greatest petroleum producers, figuring in the ninth position with approximately 3,363 thousand barrels per day in 2017. We also have the 15th largest oil reserve in the world. At the same time, as stated by Worldatlas [18], Brazil is also an important cow's milk producer with the fourth largest production in the world (around 34.3 billion kilograms annually). These two scenarios play a relevant role in economy as a whole.

Based on these facts, important government agencies, such as the Brazilian National Agency of Petroleum, Natural Gas and Biofuels (*Agência Nacional do Petróleo, Gás Natural e Biocombustíveis - ANP*), and the Brazilian Agricultural Research Corporation (*Empresa Brasileira de Pesquisa Agropecuária*), have been funding research projects and startup competitions in partnership with universities and private companies, to encourage researchers from different fields of study to implement solutions for the petroleum and dairy industries. In this context, this thesis intent to give further contributions by analyzing the employment of a well established technology (the resonant cavity sensor) in applications focused to solve problems from both, petroleum and dairy industries.

The specific topics covered in this work are listed in the next section.

1.2 SCOPE AND CONTENT OF THE THESIS

This thesis presents contributions for developments in the area of resonant frequency measurement techniques, incorporating the well established technology of resonant cavities with radiofrequency analog electronics, mainly motivated by the need of adequate sensing in specific industrial processes.

Since resonant cavity sensors are well adequate for measuring different physical quantities in a non-invasive and non-destructive way, we can formulate the hypothesis of this thesis as:

Thesis hypothesis: *It is possible to conceive a feasible and efficient measurement system combining the resonant cavity sensor technology with a sophisticated measurement technique, based on a phase-locked loop, to be employed in two specific industrial applications: water fraction determination in two phase flows in oil and gas industry, and fat content determination of bovine milk in dairy industry.*

The applications cited above have been addressed by considering (i) the modeling and analysis of a resonant frequency tracking system and (ii) the measurement setup implementation and experimental measurements using off-the-shelf components.

In the first application, the well known problem in petroleum industry, regarding multiphase flow measurement, is again investigated following the main achievements obtained in two previous studies presented in [13] and [14]. In this case, the sensor was employed for monitoring the water fraction in a gas-liquid stratified flow pattern with static measurements at the laboratory.

The second application is related to the monitoring and control of milk quality in dairy industry. In this scenario, the accurate measurement of the milk constituents (at least one tenth of the milk constituent percentage), such as fat, is mandatory in order to assure the production reliability and quality control. The fat content control is an important stage in milk production called standardization, since in general three different types of milk are produced: skimmed, semi-skimmed and whole milk, which have distinct fat contents. In large industries, mainly in developed countries, the milk production is highly automatized and several in-line measurement instruments are employed. On the other hand, in small-and medium-sized industries, specially in developing countries as in South America, there is a lack of automation and most of these

industries are still employing humans for monitoring and controlling the standardization process. As stated before, Brazil is considered one of the greatest world milk producer, however the major part of the dairy production are from small-and medium-sized industries, and as a consequence there is a need for improving the production processes. In view of this scenario, the sensor was employed for the in-line monitoring of fat content and an automatic standardization system was also proposed.

These two applications are the motivation for modeling and implementing a resonant frequency tracking system, based on a PLL approach, consisting of a resonant cavity sensor and a dedicated radiofrequency circuit. The implemented measurement system is described in detail along the thesis.

The thesis is organized in three main chapters. In Chapter 2, the electrical modeling and impedance matching analysis of the sensor are covered. The modeling and analysis of the resonant frequency tracking system are explored in Chapter 3. Finally, the employment of the sensor system is presented in Chapter 4. Conclusions and future works suggestions are drawn in Chapter 5.

2 THE RESONANT CAVITY SENSOR

In this chapter, a brief description of the physical working principle of the resonant cavity sensor developed in [13] is explored. The main results of the implemented impedance matching analysis, previously published in [19], are also explored. Finally, the mathematical modeling of the sensor is developed and validated.

2.1 WORKING PRINCIPLE

From the description of electromagnetic fields provided by Maxwell's equations [20], we can describe the propagation of electromagnetic waves, through a medium or in a vacuum, using the three-dimensional form of the wave equation, that can be written in terms of either the electric field $\mathbf{E}$

$$\nabla^2\mathbf{E} - \frac{1}{c^2}\frac{\partial^2\mathbf{E}}{\partial t^2} = 0, \tag{2.1}$$

or the magnetic field $\mathbf{B}$

$$\nabla^2\mathbf{B} - \frac{1}{c^2}\frac{\partial^2\mathbf{B}}{\partial t^2} = 0, \tag{2.2}$$

where $c = 1/\sqrt{\mu\epsilon}$ is the speed of the wave propagation, in which $\mu = \mu_o\mu_r$ and $\varepsilon = \varepsilon_o\varepsilon_r$ are the permeability and the permittivity of the medium, respectively. The constant μ_o is the magnetic permeability of free space and the variable μ_r is the relative permeability. Analogously, the constant ε_o is the permittivity of free space, while ε_r is the relative permittivity. ε_r is a complex variable, usually represented by $\varepsilon_r = \varepsilon_r^{'} + j\varepsilon_r^{''}$. If it is positive, the imaginary part stands for the losses of the medium [1], [21].

When microwaves propagate in transmission lines, their propagation is analyzed by means of a solution for the wave equation in a waveguide. There are an infinite series of solutions corresponding to two separate sets of propagation modes: Transversal Electric TE_{nm} (waves with only transverse electric fields) and Transversal Magnetic TM_{nm} (waves with only transverse magnetic fields).

Resonant cavities can be considered as a section of a hollow waveguide, built in rectangular or cylindrical shapes, and bounded by impedance discontinuities, in which the energy is stored in the electromagnetic fields at high frequencies. The resonance occurs at the frequency where the excitation field is in phase with the reflection components, resulting in a high standing wave pattern inside the cavity. This phenomenon takes place at distinct frequencies corresponding to the resonant modes TE_{nml} and TM_{nml}, where n, m, and l are integers referring to the number of electric field maxima in the standing wave pattern along the x, y, and z directions for rectangular cavities, or ϕ, r, and z directions for cylindrical cavities [1], [21].

The resonant frequency of a cylindrical cavity can be determined by [1]

$$f_{r,nml} = \frac{1}{2\sqrt{\mu\varepsilon}} \left[\left(\frac{p_{nm}}{\pi a} \right)^2 + \left(\frac{l}{d} \right)^2 \right]^{1/2}, \tag{2.3}$$

where p_{nm} are mth-order Bessel functions of the first kind, that vary according to the propagation mode, a is the cavity radius, l is related to the propagation mode, and d is the cavity length. As stated in (2.3), once the dimensions and the propagation mode are defined, the resonant frequency of a cylindrical resonant cavity sensor (RCS) is a function of the permeability and permittivity of the medium, which means that it can be sensitive to different materials under test (MUT).

The RCS presented in this thesis is formed by a PVC pipe inside a metallic cylinder (Fig. 2.1(b)) with the dimensions shown in Fig. 2.1(a). It was designed to resonate in the TE_{111} propagation mode. The space between the metallic cylinder and the PVC pipe is filled with fresh water to keep the resonance frequency between 150 MHz and 250 MHz. The frequency range and the propagation mode were chosen taking into account the dimensions of the sensor, and the losses of the effective permittivity of water (the main MUT of this work), that is negligible for frequencies below 1 GHz [22]. It is also important to highlight that the TE_{111} propagation mode, in this frequency range, is not disturbed by other propagation modes. Further details about the sensor design and its implementation can be found in [13]. Substituting the specifications above in (2.3), and considering that in this work the MUT is non magnetic ($\mu_r \approx 1$), the resonant frequency of the sensor can be expressed as

Figure 2.1: Sketch (a) and photograph (b) of the resonant cavity sensor.

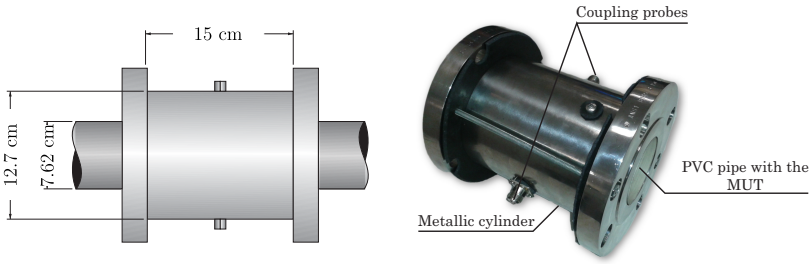

Source: The Author.

$$f_{r,TE_{111}} = \frac{1}{2\sqrt{\mu_o \varepsilon_o \varepsilon_r}} \left[\left(\frac{1.841}{\pi\ 0.0635} \right)^2 + \left(\frac{1}{0.15} \right)^2 \right]^{1/2} = \frac{k\ c_o}{\sqrt{\varepsilon_r}}, \quad (2.4)$$

where k =5.69 m^{-1} is an empirical constant (dependent on the geometry of the cavity), $c_o = 1/\sqrt{\mu_o \varepsilon_o} \approx 3 \times 10^8$ m/s is the speed of light in vacuum, and ε_r is the MUT relative permittivity.

According to (2.4), the resonant frequency is inversely proportional to the square root of the effective permittivity of the medium, which can properly vary with the MUT. This is the physical working principle of the RCS. The magnitude and/or phase of the transmission coefficient S_{21}[1] can be used as measurement parameter. Different approaches can be employed to extract this information. We will explore some of them in later chapters.

Another important parameter of the RCS is its quality factor Q. This parameter is defined as [1]

$$Q = \frac{2\pi\, Energy\, stored}{Energy\, dissipated}. \quad (2.5)$$

[1] S_{ij} are known as the *scattering parameters* of a two-port network, which is defined by the quotient of the reflected wave in port i per the incident wave in port j. It represents the forward transmission coefficient of the jth port if i is greater than j, and the reverse transmission coefficient if i is less than j [23].

This definition accounts only for the Q of the sensor itself, including the losses due to dielectric, the metal parts, and through radiation. However, to measure the resonant frequency and quality factor, the field inside the resonator must be excited by an external circuit through the coupling probes shown in Fig. 2.1(b). The waves will propagate from one coupling to the other and will be reflected in alternating directions at the discontinuities. This will "load" the resonator, which means that part of the stored energy dissipates through the coupling probes. As a consequence, the measured quality factor will be the loaded quality factor Q_l given by

$$\frac{1}{Q_l} = \frac{1}{Q_u} + \frac{1}{Q_e}, \tag{2.6}$$

where Q_u represents the unloaded quality factor, due to the losses from dielectric, metal parts, and radiation, whereas Q_e are the external Q-factor, that accounts the additional external losses when the sensor is attached to the external circuit through the coupling probes. This external Q-factor is added to the unloaded Q-factor.

Using the method of insertion loss for measuring the resonant frequency, the resonator is excited through one coupling, and the field strength is measured through the other coupling. The ratio between the received power and the incident power is the insertion loss, that depends on the Q_l and the size of the probes. Considering that the coupling probes are identical, the insertion loss IL and phase shift ϕ can be approximated by [1]

$$IL = \frac{\left(1 - \frac{Q_l}{Q_u}\right)^2}{1 + Q_l^2 \left(\frac{f}{f_r} - \frac{f_r}{f}\right)^2}, \tag{2.7}$$

and

$$\phi = \phi_0 - \arctan\left[Q_l \left(\frac{f}{f_r} - \frac{f_r}{f}\right)\right], \tag{2.8}$$

respectively, where ϕ_o can be 0° or 180° depending on the location of the couplings. In the following section, we will see how the mismatch impedance, between the sensor and the external measurement circuit, impacts the insertion loss and quality factor, and by what method this phenomenon can be avoided.

Figure 2.2: Magnitude of transmission coefficient S_{21} according to frequency for each percentage of water fraction in a stratified water/air mixture (experimental results). Note that w100% means one hundred percent of water.

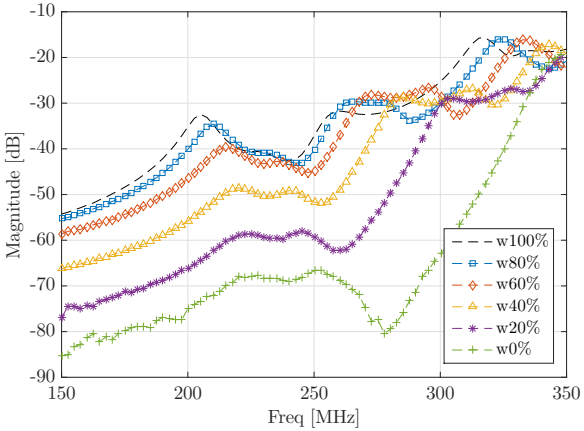

Source: The Author.

2.2 IMPEDANCE MATCHING ANALYSIS

As stated in previous section, part of the stored energy in the RCS is lost through the coupling probes. The losses can be even greater when there is a mismatch impedance between the coupling probes and external measurement circuit. Regarding the main application of the RCS (explored in 4.1), in the frequency range of the first resonant mode (TE_{111}), the magnitude of transmission coefficient S_{21} is attenuated as the water fraction decreases, when a stratified water/air mixture is present. The magnitude of S_{21}, when the water fraction decreases from 100% to 0% in a stratified water/air mixture, is shown in Fig. 2.2. We can observe that the amplitude ratio between the first and the others resonant modes gradually decreases, specially at low water fractions, where the first resonance peak almost disappears. Hence, the quality factor is also reduced, so that the first resonance becomes more noisy and inappropriate to be used as a measurement parameter. The lower the quality factor, the more uncertainty occurs in the peak identification. This signal attenuation occurs mainly due to (i) the water content decreases and (ii) by the impedance mismatch between the coupling probes and external measurement circuit. In this work we used a 50

Figure 2.3: Example of an impedance matching design for a purely resistive source Z_S and a complex impedance load Z_L, using an L network with passive components.

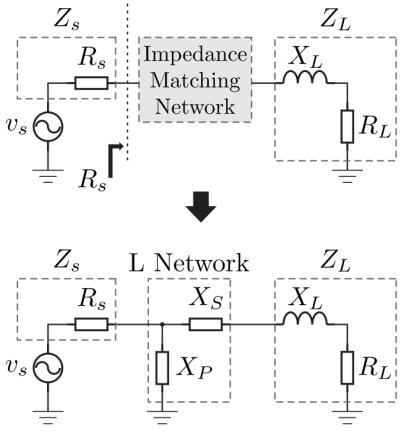

Source: The Author.

Ω based system, and to enhance the power transmission we designed impedance matching networks.

The purpose of adding an impedance matching network is to improve the power transfer between source and load. This is a common technique in several applications, as for example, in communication systems, medical applications, and applications in wireless energy transfer [24], [25], [26], [27].

Most impedance matching networks are designed taking into account reactive loads. For maximum power transfer, the primary objective in any impedance matching scheme is to transform the load impedance in the complex conjugate of the source impedance. There are different techniques to accomplish it. One of the simplest technique is to add an L network between source and load, which consists of a combination of two passive reactive components in a shunt-series or series-shunt configuration. In Fig. 2.3 is shown an example of an impedance matching design between the source and load impedances, represented by $Z_s = R_s$ and $Z_L = R_L + jX_L$, respectively. The load presents an inductive reactance, and the source is purely resistive. In this case, the values of the series component X_S and the shunt component

Figure 2.4: Setup implementation to extract the sensor's S-parameters for each percentage of water fraction using a Vector Network Analyzer (detail of the impedance matching network coupled at the sensor's port).

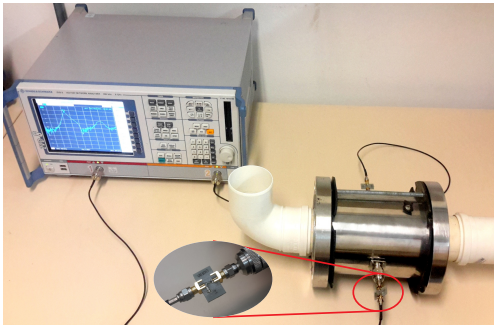

Source: The Author.

X_P are calculated as (considering $R_s > R_L$) [28]:

$$X_S = X_S^{'} + X_L, \tag{2.9a}$$

$$X_P = \frac{R_S}{Q}, \tag{2.9b}$$

$$Q = \sqrt{\frac{R_s}{R_L} - 1}, \tag{2.9c}$$

where $X_S^{'} = QR_L$, and Q is the quality factor of the circuit. Note that, in this scenario, a low-pass as well as a high-pass configuration can be implemented. The adequate choice is based on different requirements, such as the minimum number of components and their quality factors.

In order to perform the impedance matching design, we used a Vector Network Analyzer (VNA) for extracting the S-parameters information of the sensor, considering each percentage of water fraction. The setup implementation using the VNA for extracting the S-parameters after the impedance matching networks implementation is shown in Fig. 2.4. In Fig. 2.5 we can observe that the impedance of the sensor ports varies according to water fraction proportion, when measured at the resonant frequency. The real part presents a variation between 1 Ω and 1.8 Ω, whereas the imaginary part varies approximately between j8 Ω and j12 Ω. Consequently, there is an impedance mismatch between the sensor ports and the 50 Ω based external measurement circuit.

The L network designed is composed by three lumped elements, a source shunt capacitor C_1, a load series inductor L_1, and a load

Figure 2.5: The dependence of resistance and reactance of the sensor's ports on water fraction at the resonant frequency (experimental values).

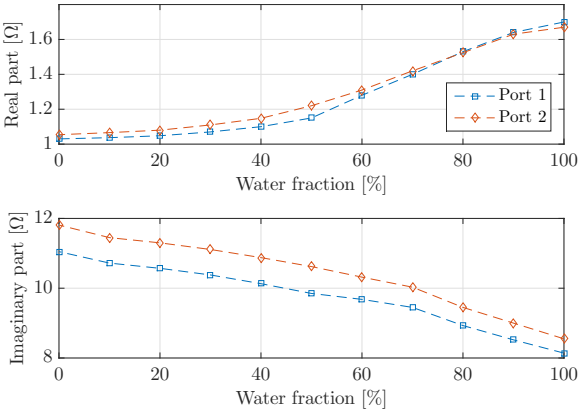

Source: The Author.

series capacitor C_2. The load series capacitor C_2 was used to reduce the inductive reactive part of the load to allow an L_1 value greater than the previous calculated because its value was in the same magnitude of the parasitic inductances. Considering $C_2 = 18$ pF and using equations (2.9) we can find the ideal values of the shunt element C_1 and the series element L_1, taking into account the load impedance and resonant frequency for each percentage of water. We used an electromagnetic model of the circuit's layout to consider the parasitic impedance of the copper paths on the substrate. All simulations were performed using the software Advanced Design System (ADS) from Agilent company, and the experimental sensor's S-parameters information for each percentage of water. Finally, we used real components for the implementation, with values near to the results obtained from simulations. A schematic diagram of the sensor with the impedance matching networks is shown in Fig. 2.6. Note that the same values are used for both impedance matching networks, since the sensor can be considered as a two port reciprocal ($S_{21} = S_{12}$) and symmetric ($S_{11} = S_{22}$) device.

A comparison between the magnitude of transmission coefficient S_{21} at the resonant frequency according to water fraction, before and after the impedance matching network implementation from simulation results, is depicted in Fig. 2.7. For the matching design, the impedance and resonant frequency values were considered for each percentage

Figure 2.6: Schematic diagram of the sensor showing the impedance matching networks.

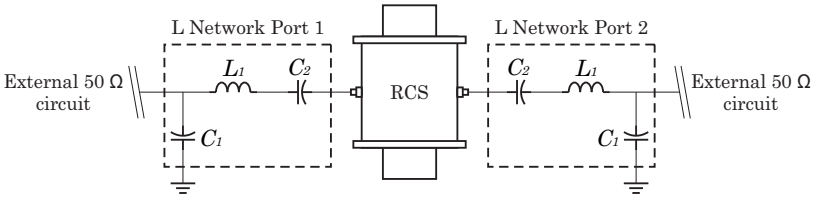

Source: The Author.

of water, and the impedance matching networks composed by ideal components. As we can observe in Fig. 2.7, the results show about 18 dB gain at high water fractions and around 22 dB gain at low water fractions. It is important to remember that there is a distinct resonant frequency for each percentage of water fraction.

The transmission coefficient for each percentage of water with the matching networks simulated on ADS are shown in Fig. 2.8 (cf. Fig. 2.2). The simulated results show that the impedance matching networks reduce the attenuation between 150 MHz and 250 MHz for the first resonant mode and strongly attenuates the other resonant modes, such that only one maximum resonant peak is now available to be reliably detected.

As it was observed from Fig. 2.5, different impedance matching networks should be implemented for each percentage of water fraction. Therefore, three impedance matching networks with fixed components, considering the impedance and frequency values for 0%, 50% and 100% of water fraction, were implemented. The values of the components are given in Table 2.1. A photograph of the implemented circuit prototypes is shown in Fig. 2.9. The simulated and experimental results of the magnitude of transmission coefficient, with and without the impedance matching networks for 0%, 50% and 100% of water fraction, are shown in Figs. 2.10, 2.11 and 2.12, respectively. As we can see, the simulated and experimental curves are correlated, mainly for 100% of water fraction. A comparison between the Maximum Available Gain (MAG)[2] and the magnitude of transmission coefficient at the resonant frequency, from

[2]The MAG is the relation between the magnitudes of the forward transmission coefficient $|S_{21}|$ and the reverse transmission coefficient $|S_{12}|$ ($MAG = |S_{21}|/|S_{12}|$), under simultaneous conjugate match conditions [29].

Figure 2.7: A comparison between the magnitude of transmission coefficient S_{21} at the resonant frequency according to water fraction, before and after the impedance matching network implementation (simulation results).

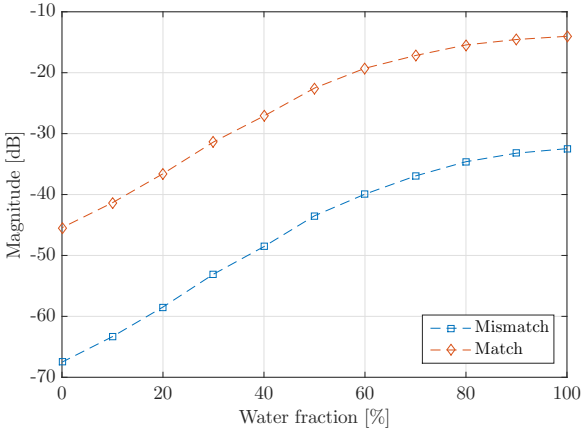

Source: The Author.

Table 2.1: Components values used in the implemented impedance matching networks.

Water fraction [%]	C_1 **[pF]**	L_1 **[nH]**	C_2 **[pF]**
0	56	18	18
50	56	22	18
100	39	33	18

the simulations (using the electromagnetic model of the circuit's layout) and experimental measurements (using the S-Parameters extract from the implemented networks), is shown in Table 2.2.

Table 2.2: Comparison between the MAG and $|S_{21}|$ from simulated/experimental results for the impedance matching implementation at the resonant frequency.

Water fraction [%]	**MAG [dB]**	$\|S_{21}\|$ **Sim. [dB]**	$\|S_{21}\|$ **Exp. [dB]**
0	-45.71	-48.98	-55.11
50	-30.40	-35.38	-39.93
100	-14.58	-21.75	-22.39

Figure 2.8: Magnitude of the transmission coefficient S_{21} according to frequency for each percentage of water fraction in a stratified water/air mixture, after the impedance matching implementation (simulation results).

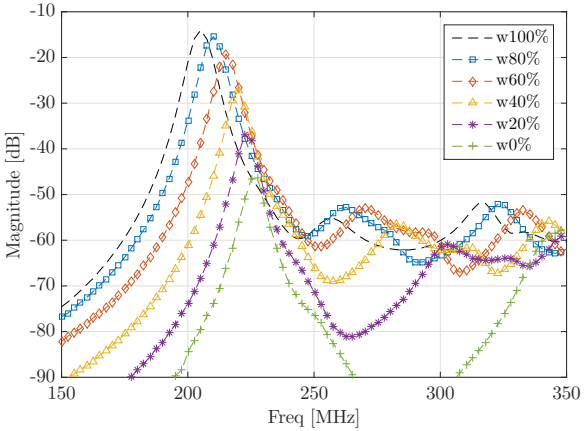

Source: The Author.

Figure 2.9: Implemented impedance matching networks for 0%, 50% and 100% cases.

Source: The Author.

From Table 2.2, it can be highlighted that for all cases, experimental and simulated results are very correlated, mainly for 100% of water fraction. The difference between the experimental results and the MAG was about 9.4 dB, for 0% and 50% of water fraction cases, and 7.81 dB for 100% of water fraction case. These results show that each passive impedance matching network, designed for 0% and 50% of water fraction, contributes with approximately 4.7 dB attenuation

Figure 2.10: Magnitude of the transmission coefficient S_{21} for 0% of water fraction.

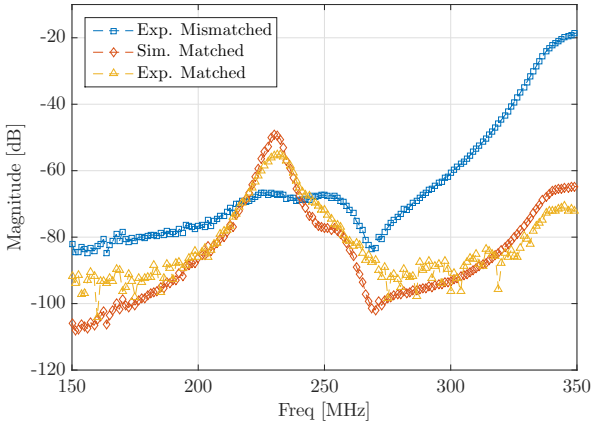

Source: The Author.

Figure 2.11: Magnitude of the transmission coefficient S_{21} for 50% of water fraction.

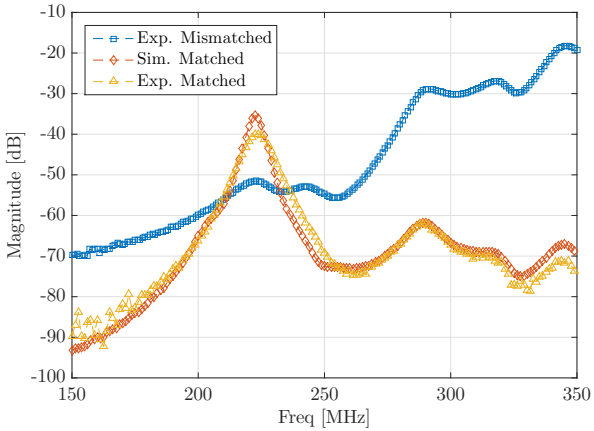

Source: The Author.

in the transmission signal, and around 3.9 dB attenuation for those impedance matching networks designed for 100% of water fraction.

We performed a Montecarlo analysis for evaluating the influence

Figure 2.12: Magnitude of the transmission coefficient S_{21} for 100% of water fraction.

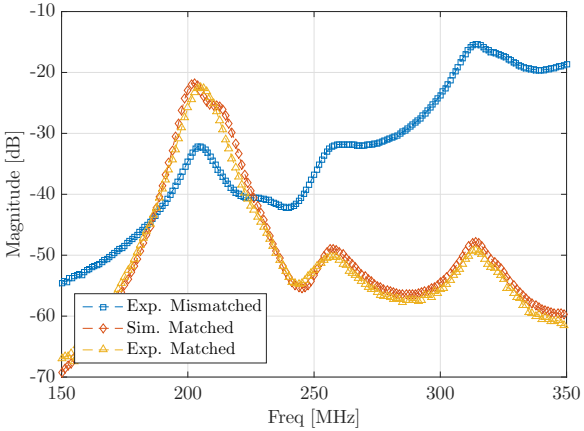

Source: The Author.

of possible variations on the impedance matching component values, which can impacts on the sensitivity of the sensor. We run 250 simulations, considering an uniform distribution over a range ±5% around the nominal component values for the case of 50% of water fraction. We observed that the standard deviation on the magnitude of the transmission coefficient at the resonant frequency was 3.5 dB. In addition, we also observed that the standard deviation around the resonant frequency was 1.53 MHz. It is important to notice that the instrument must be calibrated before the measurements, and as a consequence, the systematic errors due to component uncertainties can be avoided.

The reflection coefficient in each port, with and without the impedance matching networks for 0%, 50% and 100% of water fraction, considering the frequency range between 150 MHz and 350 MHz, are shown in Figs. 2.13, 2.14 and 2.15, respectively. The markers show the impedance at the resonant frequency before matching implementation (black circles), after matching implementation from simulation results (black triangles) and after matching implementation from experimental results (black stars). In the resonant frequency for 0% and 50% of water fraction, the real part of the impedance reaches around 30% and 40% of expected value (center of the Smith Chart), respectively, with some reactive load, whereas for 100% of water fraction the results are even better, reaching around 90% of expected value, also with some reactive

Figure 2.13: Impedance matching comparison for ports 1 and 2 in the Smith Chart for 0% of water fraction (150 MHz - 350 MHz).

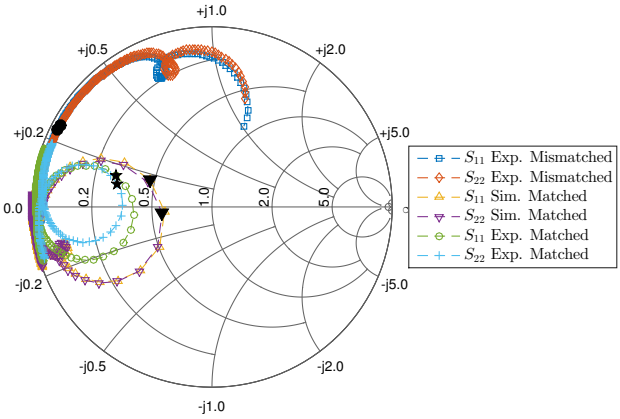

Source: The Author.

Figure 2.14: Impedance matching comparison for ports 1 and 2 in the Smith Chart for 50% of water fraction (150 MHz - 350 MHz).

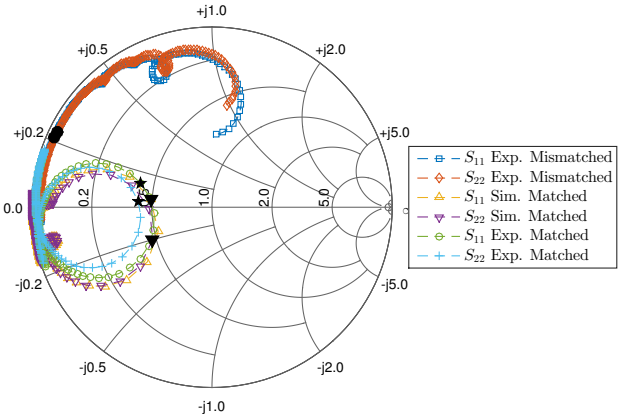

Source: The Author.

load.

In the next section, the sensor's dynamics are modeled using an electrical resonant circuit approach.

Figure 2.15: Impedance matching comparison for ports 1 and 2 in the Smith Chart for 100% of water fraction (150 MHz - 350 MHz).

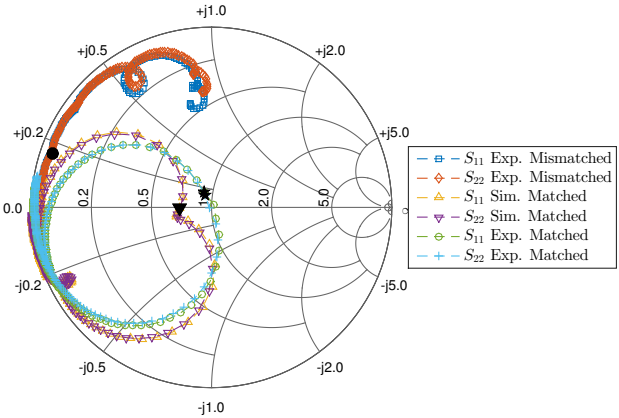

Source: The Author.

2.3 RESONANT CIRCUIT REPRESENTATION

Near to resonance, resonant cavities operating in radiofrequency or microwave ranges can be modeled as an equivalent linear resonant circuit of lumped components (RLC) in a serial arrangement [1], [21]. In this sense, we analyzed the first resonant mode of the RCS using a series RLC circuit, considering the cases of 100% and 50% of water fraction. Simulations in Matlab, using the phenomenological model, and ADS, using the experimental data from the measured S-parameters, were performed. The circuit analysis for both, mismatched and matched cases, are demonstrated in Appendix A.

The RLC circuit for the mismatched case can be modeled as depicted in Fig. 2.16. The shunt and series resistances R_1 and R_2, respectively, accounts for the losses due to metal parts and the coupling probes. The input signal u_{rcs}, is represented by a voltage source, and the loads $R_s = 50\,\Omega$, represent the external circuit impedance. The RLC model has a resonant frequency given by $\omega_r = 1/\sqrt{LC}$. Therefore, it follows from (2.4) and ω_r that the variable capacitance C can be described as a function of ε_r:

$$C = \frac{\varepsilon_r}{L}\left(\frac{1}{2\,\pi\,k\,c_0}\right)^2. \tag{2.10}$$

In frequency domain, the transfer function between $U_{rcs}(s)$ and $Y_{rcs}(s)$ is given by

$$H_{rcs}(s) = \frac{Y_{rcs}(s)}{U_{rcs}(s)} = \frac{\alpha s}{s^2 + 2\xi\omega_r s + \omega_r^2}, \tag{2.11}$$

where $\alpha = R^2/(R_s L)$ is a constant, $\omega_r = 1/\sqrt{LC}$ is the natural oscillation frequency, $R = (R_1 R_s)/(R_1 + R_s)$, and $\xi = (R_2 + R)C/\sqrt{LC}$ is the damping coefficient.

The transfer function (2.11) describes the behavior of the first resonant mode (TE111) of the RCS in frequency domain. In addition, the values of R_1, R_2, and C change as the water fraction on the system decreases, since the insertion loss and quality factor of the first resonant mode depends on the water fraction, as shown in Fig. 2.2. Henceforth, besides the RCS's intrinsic dynamics, there is an extra dynamics regarding the MUT variation, leading to a complete description of the sensor's behavior.

Figure 2.16: RCS's model for the first resonant mode, using a series RLC circuit.

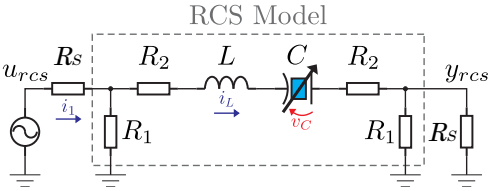

Source: The Author.

From the frequency response analysis, shown in Fig. 2.17, we can observe that magnitude and phase from measured data are in agreement with the RLC model results. As expected, the phase response of the RCS model starts at 90°, since (2.11) has a zero at the origin of the complex plane. In the resonance, the phase is zero and at high frequencies it converges to −90°. The phase response of the ADS simulation starts at −90°. This occurs because when a single type of excitation coupling is used, the resonant cavity phase is shifted by 0° or 180° [1] (as stated in Section 2.1), which means that, in this case, the RCS's phase is 180° delayed ($\phi_0 = -180°$ in 2.8), and this phase shift is not considered in the RLC model. For this reason, we added 180° to the phase data from ADS simulation in Fig. 2.17 to properly compare both, RLC model and ADS results. This 180° phase shift will not be a problem for the control design, as we will see in Chapter 3. As previously explained, the RLC model only considers the first resonant mode, therefore for high frequencies (in this case, frequencies greater than 220 MHz) the RLC model has no correlation with the ADS simulation, as we can observe in Fig. 2.17.

The RCS model presented above does not take into account the impedance matching networks. With such impedance matching networks, the measurement's reliability is improved, since they enhance the power transfer of the system and the first resonant mode can be properly identified, as demonstrated in Section 2.2. We also verified that the input impedance depends on the frequency and water fraction variations. Hence, we used the impedance matching networks designed for 100% of water fraction, since this approach provided better results when compared with the other impedance matching networks (designed for the 0% and 50% cases). The later projects were not suitable for measuring in a full range (0% to 100%) of water fraction, since the resonant frequency

Figure 2.17: Frequency response for the RCS model validation.

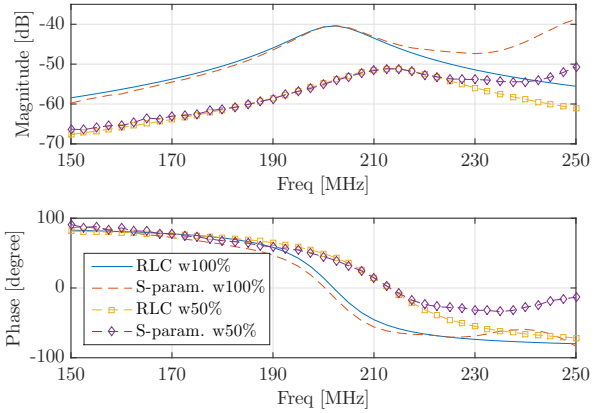

Source: The Author.

of the first resonant mode did not present a sufficient variation to be tracked. One important examination is that using the impedance matching networks, the additional resonant modes are attenuated, and the mathematical model becomes more trustworthy. The RCS model with the impedance matching networks (IMN P1 and IMN P2), is show in Fig. 2.18.

Figure 2.18: Series RLC model of the resonant cavity sensor including the impedance matching networks.

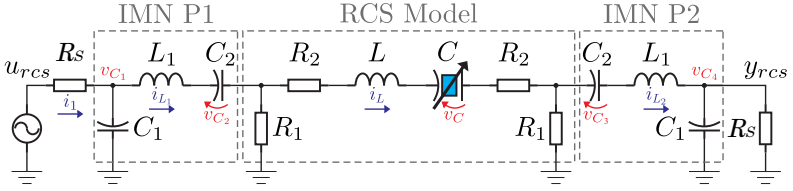

Source: The Author.

The eighth order transfer function relating $U_{rcs}(s)$ with $Y_{rcs}(s)$ for frequency domain analysis will have the form

$$H_{rcs}(s) = \frac{Y_{rcs}(s)}{U_{rcs}(s)} = \frac{CC_2^2R_1^2R_s s^3}{\prod_{i=1}^{8}(s+p_i)}, \tag{2.12}$$

Table 2.3: Numerical values for both, mismatched and matched, RCS models.

	w100% Mismatch	w50% Mismatch	w100% Match	w50% Match
L [nH]	80	80	80	80
R_1 [Ω]	2	1.3	1.6	1.2
R_2 [Ω]	1.95	4.5	7	20
f_r [MHz]	202	213	204	208
C_1 [pF]	-	-	92.9	102.33
C_2 [pF]	-	-	41.65	49.82
L_1 [nH]	-	-	20.82	17.72
Z1	0	0	0	0
Z2, Z3	-	-	0	0
P1, P2	$(-0.05 \pm 1.27\text{i}) \times 10^9$	$(-0.07 \pm 1.33\text{i}) \times 10^9$	$(-0.12 \pm 1.3\text{i}) \times 10^9$	$(-0.27 \pm 1.28\text{i}) \times 10^9$
P3, P4	-	-	$(-0.056 \pm 1.29\text{i}) \times 10^9$	$(-0.063 \pm 1.3\text{i}) \times 10^9$
P5, P6	-	-	$(-0.07 \pm 1.3\text{i}) \times 10^9$	$(-0.065 \pm 1.3\text{i}) \times 10^9$
P7, P8	-	-	-0.15×10^9	-0.13×10^9

where the zeros, and poles values are given in Table 2.3, besides all the components values used considering 100% and 50% of water fraction for both, mismatched and matched RCS models. These values were empirically determined based on the experimental measurements using the VNA, where the components were adjusted for the experimental response compatibility.

The frequency response comparison for both cases, 100% and 50% of water fraction, is depicted in Fig. 2.19. Here, we clearly can observe the expected influence of the impedance matching networks on the phase response. In the frequency range analyzed, between 150 MHz and 250 MHz, the phase dynamics starts around 90°, with the resonance approximately at −180°, and finally converging to −400° at 250 MHz. At low frequencies, the zeros introduce a positive phase shift of approximately 270°. As a consequence, the poles and zeros of the system introduce a total phase shift of 720° from low to high frequencies.

It is also notable, that for the case of 50% of water fraction the experimental and simulated values in phase graphic are less correlated. One possible reason for this behavior is that the impedance matching networks were designed for the case of 100% of water fraction, which implies that the impedance matching results is less effective and the networks influence the phase response.

The impedance matching correspondence for the sensor's input using the Smith Chart in the range from 150 MHz to 250 MHz is exhibited in Figs. 2.20 and 2.21, for 100% and 50% of water fractions, respectively, where the blue inverted triangle and the red star markers correspond to the simulated RLC model and S-parameter impedance values at resonance, respectively. It is evident that the RLC model and the experimental S-parameters results are in good agreement.

Figure 2.19: Frequency response for the RCS model validation including the impedance matching networks.

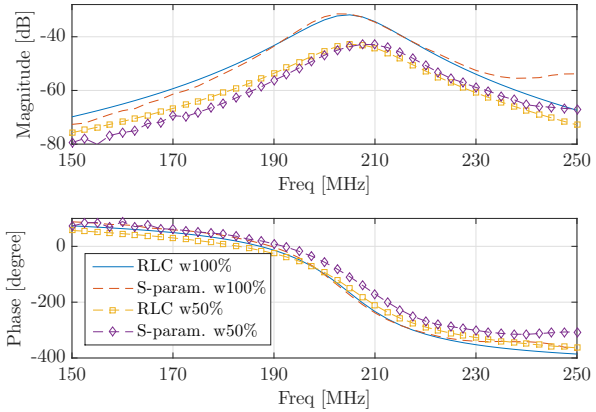

Source: The Author.

Figure 2.20: Impedance matching comparison for the RCS model validation considering 100% of water fraction.

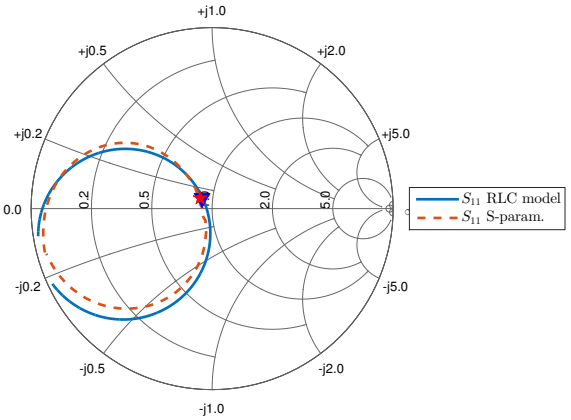

Source: The Author.

Figure 2.21: Impedance matching comparison for the RCS model validation considering 50% of water fraction.

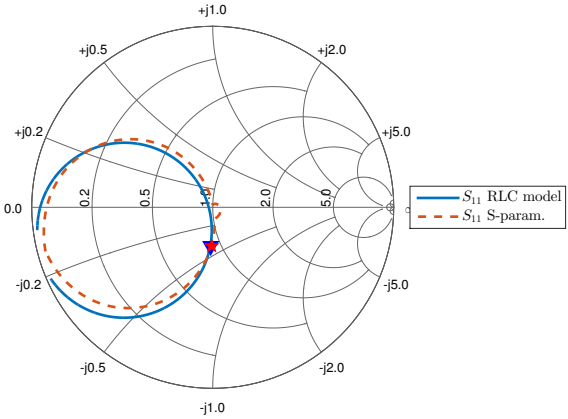

Source: The Author.

2.4 SUMMARY

The physical working principle of the RCS is based on the MUT permittivity variation, and the magnitude as much as phase information at resonance can be used as measurement parameters. The suitable impedance matching, between the sensor and the external measurement circuit, is mandatory to improve the reliability of the measurement system. Three pairs of impedance matching networks were implemented, taking into account the cases of 0%, 50% and 100% of water fraction. Based on the applications addressed in this work, we concluded that the ones desined for the case of 100% of water fraction were adequate for the measurements improvement. The sensor dynamics can be well described by a second order linear resonant circuit, however the results without using the impedance matching networks can be slightly different, since the model considers only the first resonant mode. The presence of the impedance matching networks attenuates the remaining resonant modes, improving the reliability of the modeling, although six additional states are introduced, increasing the complexity of the system. The RCS model, including the impedance matching networks, provides a whole description of the sensor's dynamics.

3 THE RESONANT FREQUENCY TRACKING SYSTEM

3.1 INTRODUCTION

The working principle of the RCS as part of a measurement system can be explained in Fig. 3.1. In the passive stage, the effective permittivity of the MUT ε_m inside the RCS's pipe varies according to a specific parameter. Then, in the active stage, the resonant frequency of the cavity, according to the effective permittivity, is measured by an external circuit using the amplitude and/or phase information of the transmission signal. Finally, the information is processed by a Digital Signal Processing (DSP) stage and associated to the desired measurement parameter.

In [30] a spectrum analyzer and a software application were employed for tracking the resonant frequency based on the amplitude of the transmission signal. This technique can be accomplished by seeking the peak of the resonance curve or by calculating the curve derivative, that is zero at the peak [1]. However, this method can be time consuming if the frequency range is large. In addition, if the quality factor of the cavity is low, the peak searching may be affected, resulting in large uncertainty in the measurements. Furthermore, laboratory instruments, such as spectrum analyzers, are expensive and, for industrial applications, they should be replaced by embedded circuits. In [2] an RF circuit based on active resonance measurement methods was implemented for the in-line measurements of granular dielectric material weight using an RCS. In this method, the RCS is part of an oscillator circuit. Although this method is simple and effective, there are some shortcomings, such as the strong dependence of all components in the circuit, once the RCS is part of the oscillator.

Alternatively, the resonant frequency can be found using the phase signal information. Considering the phase method, a solution for automatic resonance tracking is the usage of Phase-Locked Loop (PLL). Techniques based on PLL have been applied on different resonant sensors, such as in Microelectromechanical and Nanoelectromechanical Systems (MENS/NEMS) for measuring density and viscosity of fluids [8], [9], and detection of carbon nanoparticles [31]. In [32], [33], [11], and [34] different control strategies are implemented for MEMS and

Figure 3.1: Block diagram of a measurement system used the RCS.

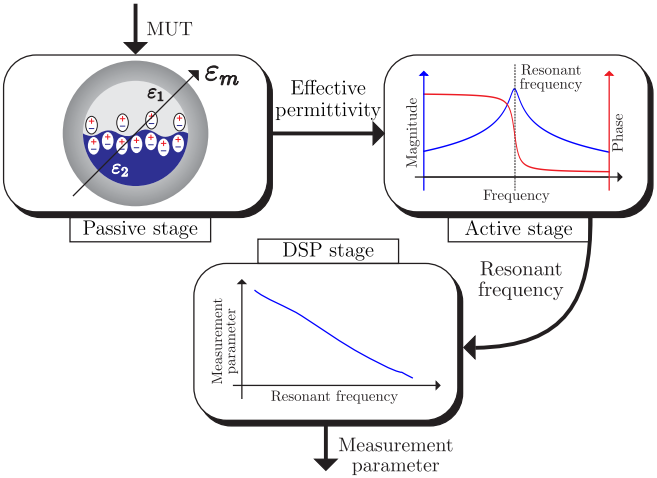

Source: The Author.

NEMS structures based on PLL. Another kind of resonant sensors for monitoring vital signs for health research [35], [36], and the measurement of physical quantities such as force [5], and temperature [6], also use resonant frequency tracking systems based on PLL.

In [37] they present simulated and experimental results about the implementation of a dual PLL, using a phase-sensitive detector, applied to a vortex-shedding flow-meter. Disturbances caused by high level of distortion on currents and voltages in power systems also have been investigated, and solutions employing PLL have been reported, in [38] and [39].

A comparative table of the technologies mentioned above and their measurement methods is shown in Table 3.1, where we can properly identify the new approach explored in this thesis.

Table 3.1: A comparative table of some technologies and their measurement methods in the state of the art.

Author	Sensor	Application	Measurement technique
Al-Hajeri et. al (2009) [30]	RCS	Monitoring of the percentage volumes of each phase of three phase flow (oil, gas, and water).	Maximum peak search (magnitude of transmission signal) using a spectrum analyzer.
Ming Huang et. al (2008) [2]	RCS	Determination of granular dielectric materials weight.	Active resonance measurement method.
O. Cakmak et. al (2015) [8], Benjamin A. Bircher et. al (2016) [9]	MEMS	Density and viscosity measurement.	PLL
Hutomo S. Wasisto et. al (2014) [31]	MEMS	Detection of carbon nanoparticles.	PLL
C. Kharrat et. al (2009) [32], H. Sohanian-Haghighi et. al (2012) [33], Byung Su Chang et. al (2007) [11], A. Kumar et. al (2015) [34]	MEMS/NEMS	Study of different control strategies.	PLL
Yunseog Hong et. al (2014) [35], S. Kim et. al (2015) [36]	RF wearable resonator	Monitoring of vital signs.	PLL
Christine Barthod et. al (2003) [5]	Double ended tuning fork sensor (DETF)	Force measurement.	PLL
Soon-Young Hong et. al (2015) [6]	Surface Acoustic Wave (SAW)	Temperature measurement.	PLL
D. W. Clarke and T. Ghaoud (2003) [37]	Vortex-shedding flow meter	Flow rate measurement.	Dual PLL
This thesis	RCS	Determination of water fraction in two-phase stratified flow regimes in petroleum industry and determination of total solids and fat contents in dairy industry.	PLL

In this Chapter, is described an automatic Resonant Frequency Tracking System (RFTS), using the Resonant Cavity Sensor previously analyzed in Chapter 2. The method is based on a PLL and a dedicated RF circuit is implemented using off-the-shelf components. The PLL based method applied to the RFTS using an RCS is an important contribution of this thesis, once it provides the combination of a consecrated system with a sophisticated measurement technique for monitoring physical quantities in petroleum and dairy industries. One of the advantages of this approach is the tracking of the resonant frequency without scanning all the RCS operational frequency range. Another important characteristic is the feasibility of implementing different control strategies with the purpose of improving the accuracy and time response of the system, since the controller is digital. Furthermore, the phase information, as well as the magnitude information, can be used to infer the measurement parameter, enhancing the robustness of the system. A theoretical description of the system is developed. The proposed technique is validated and experimental results are analyzed.

3.2 SYSTEM OVERVIEW

The phase-locked loop is essentially a feedback control system that synchronizes a harmonic output signal with a harmonic reference signal, in frequency and in phase. In Fig. 3.2 is shown a classic PLL block diagram. Basically, it consists of a phase detector (PD), a controller, and a voltage controlled oscillator (VCO). The PD detects the phase difference between the reference and output signals, and the VCO frequency is controlled based on the phase error between them. In the locked state, the phase error is brought to zero, or remains at a constant value [40].

Figure 3.2: Classic PLL block diagram.

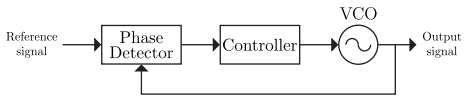

Source: The Author.

The Resonant Frequency Tracking System presented in this thesis is based on a PLL configuration. The simplified RFTS block diagram is depicted in Fig. 3.3, where the dotted lines correspond to

Figure 3.3: Simplified RFTS block diagram.

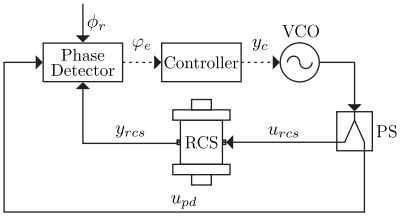

Source: The Author.

phase/frequency signals, while the solid lines correspond to harmonic signals. In this case, the VCO output signal is converted, using a power splitter (PS), in two new signals, u_{rcs} and u_{pd}, that are sent to the RCS and PD inputs, respectively. The voltage signal u_{pd} is considered as a reference signal, that is based on the VCO output, incorporating an specific phase reference value ϕ_r (generally related to the RCS's resonant frequency). This phase reference value is added to the reference signal for control purposes, and as it will be demonstrated later in this chapter, this constant is used to assure a correct resonant frequency tracking of the system. The amplitude and phase of the RCS's output signal y_{rcs} vary according to the MUT permittivity inside the sensor. The PD calculates the phase error φ_e between ϕ_r and the resultant phase shift φ, that can be considered as the system phase output. Finally, the controller sets the VCO frequency by means of the control signal y_c, leading φ_e to zero. In this frequency, the system is locked at the resonance or near to it from a constant offset.

In the ideal case, u_{rcs} and u_{pd} have the same amplitude and phase, but if we consider a more detailed conception of the simplified block diagram shown in Fig. 3.3, we have

$$u_{rcs}(t) = \hat{u}_{rcs}\cos(\varphi_{vco}(t) + \Delta\phi_{rcs}), \tag{3.1a}$$

$$u_{pd}(t) = \hat{u}_{pd}\cos(\varphi_{vco}(t) + \Delta\phi_{pd} + \phi_r), \tag{3.1b}$$

where $\Delta\phi_{rcs}$ and $\Delta\phi_{pd}$ are constant values denoting the phase shift generated by the RF cables and components. The VCO phase is given by the integral of the VCO frequency ω_{vco}, i.e.,

$$\varphi_{vco}(t) = \int_0^t \omega_{vco}(\tau)d\tau, \tag{3.2}$$

and in turn ω_{vco} is controlled by the control signal y_c as follows

$$\dot{\varphi}_{vco}(t) = \omega_c + K_{vco}\, y_c(t), \tag{3.3}$$

where ω_c is the center oscillating frequency [rad/s], and K_{vco} is the VCO's gain [rad/(sV)].

Taking into account a linear model of the RCS, the output signal is represented as

$$y_{rcs}(t) = \hat{y}_{rcs}(t)\cos(\varphi_{rcs}(t)), \tag{3.4}$$

whose the phase shift reads

$$\varphi_{rcs}(t) = \varphi_{vco}(t) + \Delta\phi_{rcs} + \Delta\varphi(t), \tag{3.5}$$

where $\Delta\varphi(t)$ and $\hat{y}_{rcs}(t)$ represent the phase and magnitude dynamics, respectively, caused by a suddenly change in the resonant frequency.

If we consider a multiplier phase detector with a low pass filter, the information regarding the phase difference between two harmonic signals is hidden in the DC term that can be consider as the cosine of the phase difference between these signals. For now, we can assume the phase detector has an ideal response given by

$$\begin{aligned} \varphi_e(t) &= K_{pd}[\varphi_{rcs}(t) - (\varphi_{vco}(t) + \Delta\phi_{pd} + \phi_r)] \\ &= K_{pd}[\Delta\varphi(t) - \phi_r + \Delta\phi_{rcs} - \Delta\phi_{pd}], \end{aligned} \tag{3.6}$$

where K_{pd} is a constant gain.

The phase error $\varphi_e(t)$ is the controller input and the controller output y_c varies the VCO frequency ω_{vco} bringing φ_e to zero. Note that in steady state, $\Delta\varphi(\omega_{vco}) \to \phi_r - \Delta\phi_{rcs} + \Delta\phi_{pd}$.

The above description is an overview of the RFTS behavior, and the ideal phase detector response will be used later in the linearized model.

The phase detector is one of the most important element of the system, since it influences the system response. There are many different ways to design such component, for instance, using analog multipliers, and also adopting digital circuits, such as XOR gates, and *flip-flops* [40]. The multiplier is the most common analog PD implementation. When two harmonic signals are multiplied, the resulted signal is build up of a

DC term, containing the desired information, besides higher-frequency terms that can be afterwards eliminated by a low-pass filter. The main limitation of this PD configuration is its phase range, since it can only detect the phase deviation in the linear interval within $-45°$ to $45°$. Hence, to overcome this condition a so-called quadrature phase detector can be used. It consists of two multipliers, in which the signals are multiplied in phase and 90° out of phase, to obtain the *in-phase* and *quadrature-phase* components of the resulted multiplication. Holding this configuration, we can acquire the phase from $-180°$ to $180°$, besides the magnitude information.

Two versions of the RFTS were implemented and validated. The first one uses a single mixer forming a multiplier phase detector, while the second version consists of a more sophisticated approach based on a quadrature phase detector. The detailed block diagrams of the RFTS for the first (a) and second (b) versions are shown in Fig. 3.4. The discrete signals are shown in gray scale, after and before the analog to digital converter (A/D) and digital to analog converter (D/A), respectively. All the modeling described in this chapter relies on the second version, since it comprises the improvements regarding the quadrature circuit. However, the working principle is basically the same, once both circuits are inherently developed to track the sensor's resonant frequency.

In Fig. 3.4(b) the VCO output signal is converted in two signals by the power splitter PS1. One of them, u_{rcs}, is amplified using a power amplifier PA, and sent to the RCS input. The other signal, u_{pd}, is sent to a hybrid port (HYB) that converts the input signal in two signals, being one of them u_{pdi}, sent *in-phase* to the (LO) input of a passive mixer MIX1, and the other one u_{pdq}, sent 90° out of phase (*quadrature*) to the LO input of a second passive mixer MIX2. The RCS output signal is splitted (PS2) and the two new signals (y_{rcs}) are sent to the RF input of MIX1 and MIX2. The mixers generate (in the IF output) two DC signals with high frequencies components, that are subsequently filtered by low pass filters LPF1 (y_{pdi}) and LPF2 (y_{pdq}). These signals are digitally processed on a computer to obtain the phase information (φ), which is used to implement the controller. A discrete-time controller is implemented in order to track a phase reference value (ϕ_r), generally corresponding to the RCS resonant frequency. The first version depicted in Fig. 3.4(a) works in an analogous way, while the main difference relies on the phase error estimative, that in this case is proportional to the cosine of the phase error between y_{rcs} and u_{pd} signals. This last approach cannot estimate the exact phase error, nor the magnitude information.

Figure 3.4: RFTS block diagrams (closed loop analysis) employing (a) a multiplier PD (first version of the implemented system), and (b) a quadrature PD (second version of the implemented system).

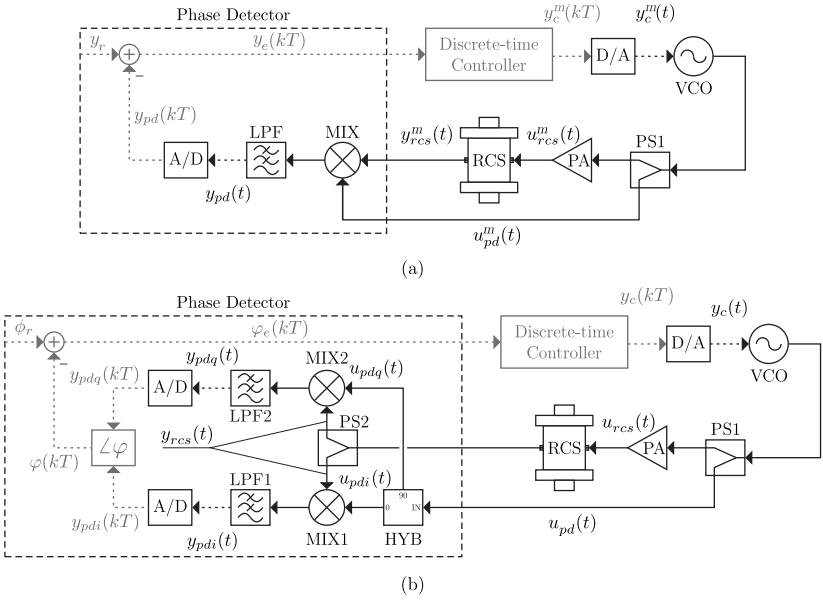

Source: The Author.

In summary, the RFTS is actually a modified PLL system, where the control signal y_c is a low frequency voltage that controls the VCO frequency, allowing the system to track the RCS's resonant frequency. The sensor stands in the feedback way before the phase detector. This is the working principle of the implemented RFTS. In the following sections, the open loop and closed loop mathematical modeling of such framework are described.

3.3 OPEN LOOP DESCRIPTION

The RFTS of Fig. 3.4(b) can be analyzed using a semi-empirical model, where the parameters values are obtained from experimental measurements. We start our analysis investigating first the system open loop dynamics. In this case, the RCS and PD blocks (see Fig. 3.4) are

the most important components, once their behavior will shape the system response.

3.3.1 Resonant Cavity Sensor Dynamics

In section 2.2, we analyzed the issues regarding the impedance matching between the sensor and the external circuit, and in section 2.3 we validated the mathematical modeling with and without the impedance matching networks. Henceforth, the impedance matching networks, designed for the case of 100% of water fraction, are used for improving the reliability of the measurements.

Despite of the influence that the impedance matching networks have in the sensor dynamics, the extra poles from the networks will not play a significant role in the analysis, although the phase response will present a larger variation from low to high frequencies, this fact does not have a great influence on the controller design, as it will be clear in Section 3.6. On the other hand, the additional poles could notably increase the model complexity which is not necessary, as we will examine later. Consequently, for modeling purposes we can assume the sensor has only one resonant mode, as in the matched case, and only two conjugated complex poles, as in the mismatched case. Therefore, the RCS's dynamics is based on (2.11), considering the zero in the transfer function can be neglected. Furthermore, as summarized in previous chapter, a low-frequency model must be employed concerning the MUT permittivity dynamics. As a consequence, (2.11) can be rewritten as

$$H_{rcs}(s) = \frac{Y_{rcs}(s)}{U_{rcs}(s)} = \frac{K_n}{s^2 + 2\xi\omega_r s + \omega_r^2}, \tag{3.7}$$

where K_n is a constant value. The low-frequency model is only valid in the sensor's operational frequency range, as it will be demonstrated in Section 3.6.2.

Applying the inverse Laplace transform in (3.7), we can represent the sensor dynamics using the most common second order differential equation

$$\ddot{y}_{rcs}(t) + 2\xi\omega_r\dot{y}_{rcs}(t) + \omega_r^2 y_{rcs}(t) = K_n u_{rcs}(t). \tag{3.8}$$

Considering a harmonic excitation $u_{rcs}(t) = \hat{u}_{rcs}\mathrm{e}^{\mathrm{j}\omega t}$, the steady state response will have the form $y_{rcs}^{ss}(t) = \hat{y}_{rcs}^{ss}e^{j(\omega t - \Delta\varphi)}$.

Therefore, in the frequency domain, the magnitude and phase of (3.7) are formulated as

$$\hat{y}_{rcs}^{ss}(\omega) = |H_{rcs}| = \sqrt{\frac{1}{(\omega_r^2 - \omega^2)^2 + (2\xi\omega_r\omega)^2}}, \tag{3.9a}$$

$$\Delta\varphi(\omega) = \angle(H_{rcs}) = -\arctan\left(\frac{2\xi\omega_r\omega}{\omega_r^2 - \omega^2}\right). \tag{3.9b}$$

As stated before in Chapter 2, the resonant frequency ω_r varies according to the MUT's effective permittivity, and as a consequence, the magnitude and phase represented in (3.9) will also change.

3.3.2 Quadrature Phase Detector Dynamics

We previously analyzed, in a simplified way, the phase detector considering an ideal response. Now, a more precise model regarding the quadrature phase detector is explored. The first step for the modeling of the quadrature phase detector is to analyze the *in-phase* (y_{pdi}) and *quadrature* (y_{pdq}) PD signals, taking into account the RCS's operating frequency range. This task is achieved by implementing an open loop VCO frequency sweep. In Fig. 3.5 is depicted the block diagram with respect to time domain signals involved in this analysis. The phase lags produced in each path from the VCO output up to the mixers and RCS inputs are represented by the constants $\Delta\phi_q$, $\Delta\phi_i$, and $\Delta\phi_{rcs}$, respectively, while the signal magnitudes are given by $\hat{u}_{pdq}$, $\hat{u}_{pdi}$, and $\hat{u}_{rcs}$.

Figure 3.5: RFTS block diagram (open loop analysis).

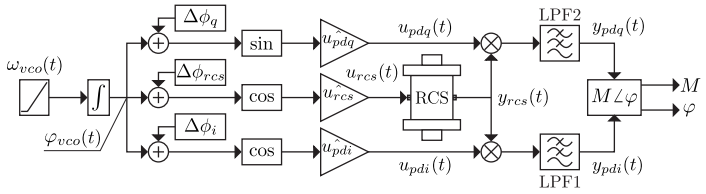

Source: The Author.

The harmonic signals involved in the analysis are described as

$$u_{pdq}(t) = \hat{u}_{pdq}\sin(\varphi_{vco}(t) + \Delta\phi_q), \tag{3.10a}$$
$$u_{pdi}(t) = \hat{u}_{pdi}\cos(\varphi_{vco}(t) + \Delta\phi_i), \tag{3.10b}$$
$$u_{rcs}(t) = \hat{u}_{rcs}\cos(\varphi_{vco}(t) + \Delta\phi_{rcs}). \tag{3.10c}$$

Considering eqs. (3.4) and (3.5), the resulted y_{pdq} and y_{pdi} signals, without the low-pass filter (LPF), are given by

$$\begin{aligned} y_{pdq}(t) &= \frac{\hat{u}_{pdq}\hat{y}_{rcs}(t)}{2}\Big[\sin(\varphi_{vco}(t) + \Delta\phi_q - \varphi_{rcs}(t)) + \sin(\varphi_{vco}(t) \\ &+\Delta\phi_q + \varphi_{rcs}(t))\Big], \\ y_{pdi}(t) &= \frac{\hat{u}_{pdi}\hat{y}_{rcs}(t)}{2}\Big[\cos(\varphi_{vco}(t) + \Delta\phi_i - \varphi_{rcs}(t)) + \cos(\varphi_{vco}(t) \\ &+\Delta\phi_i + \varphi_{rcs}(t))\Big]. \end{aligned} \tag{3.11}$$

By substituting (3.5) into (3.11), and considering that the high frequency terms are filtered out by the low-pass filter, y_{pdq} and y_{pdi} signals can be approximated by

$$y_{pdq}(t) \approx \frac{\hat{u}_{pdq}\hat{y}_{rcs}(t)}{2}\sin(-\Delta\varphi(t) - \Delta\phi_{rcs} + \Delta\phi_q), \tag{3.12a}$$
$$y_{pdi}(t) \approx \frac{\hat{u}_{pdi}\hat{y}_{rcs}(t)}{2}\cos(-\Delta\varphi(t) - \Delta\phi_{rcs} + \Delta\phi_i). \tag{3.12b}$$

Making the assumptions that $\cos(-\Delta\varphi(t) - \Delta\phi_{rcs} + \Delta\phi_i) = \sin(\Delta\varphi(t)+\Delta\phi_{rcs}-\Delta\phi_i+\pi/2)$, and assuming only small phase variations, we can use the small angle approximation ($\sin(a) \approx a$) to simplify (3.12) as

$$y_{pdq}(t) \approx \frac{\hat{u}_{pdq}\hat{y}_{rcs}(t)K_q}{2}\Big(-\Delta\varphi(t) - \Delta\phi_{rcs} + \Delta\phi_q\Big), \tag{3.13}$$
$$y_{pdi}(t) \approx \frac{\hat{u}_{pdi}\hat{y}_{rcs}(t)}{2}\Big(\Delta\varphi(t) + \Delta\phi_{rcs} - \Delta\phi_i + \pi/2\Big), \tag{3.14}$$

where K_q is a constant required due to the small angle approximation. Despite the presence of $\pi/2$ in (3.14) the sum of all phase shifts in

the argument will have a small value, assuring the small phase angle approximation as we will see later in section 3.6.

These resulted signals represent the real and imaginary part of a complex number with magnitude:

$$M = \sqrt{y_{pdq}^2 + y_{pdi}^2}, \tag{3.15}$$

and a phase shift φ calculated by the atan2[1] function:

$$\varphi(y_{pdq}, y_{pdi}) = \text{atan2}(y_{pdq}, y_{pdi}). \tag{3.16}$$

Applying the Laplace transform in (3.14), and in view of the dynamics of a first order low-pass filter, we have

$$Y_{pdq}(s) = \frac{\hat{U}_{pdq}}{2}\hat{Y}_{rcs}(s)K_q(-\Delta\Phi(s) - \Delta\Phi_{rcs} + \Delta\Phi_q)H_{lp}(s), \tag{3.17a}$$

$$Y_{pdi}(s) = \frac{\hat{U}_{pdi}}{2}\hat{Y}_{rcs}(s)(\Delta\Phi(s) + \Delta\Phi_{rcs} - \Delta\Phi_i + \pi/2)H_{lp}(s), \tag{3.17b}$$

with

$$H_{lp}(s) = \frac{\omega_g}{s + \omega_g}, \tag{3.18a}$$

where ω_g is the low-pass filter cut-off frequency.

Finally, substituting (3.18) in (3.17), and applying the inverse Laplace transform, we obtain the differential equations of the *quadrature* and *in-phase* signals

$$\dot{y}_{pdq}(t) = \omega_g \left[\frac{\hat{u}_{pdq}}{2}\hat{y}_{rcs}K_q(-\Delta\varphi(t) - \Delta\phi_{rcs} + \Delta\phi_q) - y_{pdq}(t) \right], \tag{3.19a}$$

$$\dot{y}_{pdi}(t) = \omega_g \left[\frac{\hat{u}_{pdi}}{2}\hat{y}_{rcs}(\Delta\varphi(t) + \Delta\phi_{rcs} - \Delta\phi_i + \pi/2) - y_{pdi}(t) \right]. \tag{3.19b}$$

[1]The function atan2 can be defined for all $(y, x) \neq (0, 0)$ most conveniently by selecting as co-domain $(-\pi, \pi]$ for the principal branch of the complex argument function applied to the complex number $x + iy$ [41].

3.3.3 State space representation

Consider that the RCS's input signal in (3.8) is a forced harmonic input given by $u_{rcs}(t) = \hat{u}_{rcs}\mathrm{e}^{\mathrm{j}(\varphi_{vco}(t)+\Delta\phi_{rcs})}$. As described in [42], the phase dynamics of a forced linear oscillator with a single degree of freedom, as the one represented by (3.8), can be investigated in terms of magnitude $\hat{y}_{rcs}(t)$, and phase angle $\varphi_{rcs}(t)$, by extending the variable $y_{rcs}(t)$ into the domain of complex numbers

$$\begin{aligned} y_{rcs} &= \hat{y}_{rcs}\mathrm{e}^{\mathrm{j}\varphi_{rcs}}, \\ \dot{y}_{rcs} &= (\dot{\hat{y}}_{rcs} + \mathrm{j}\hat{y}_{rcs}\dot{\varphi}_{rcs})\mathrm{e}^{\mathrm{j}\varphi_{rcs}}, \\ \ddot{y}_{rcs} &= (\ddot{\hat{y}}_{rcs} - \hat{y}_{rcs}\dot{\varphi}_{rcs}^2 + \mathrm{j}(\hat{y}_{rcs}\ddot{\varphi}_{rcs} + 2\dot{\hat{y}}_{rcs}\dot{\varphi}_{rcs}))\mathrm{e}^{\mathrm{j}\varphi_{rcs}}. \end{aligned} \tag{3.20}$$

Substituting (3.20) in (3.8), we obtain

$$\begin{aligned} &[\ddot{\hat{y}}_{rcs} - \hat{y}_{rcs}\dot{\varphi}_{rcs}^2 + \mathrm{j}(\hat{y}_{rcs}\ddot{\varphi}_{rcs} + 2\dot{\hat{y}}_{rcs}\dot{\varphi}_{rcs}) + 2\xi\omega_r(\dot{\hat{y}}_{rcs} + \mathrm{j}\hat{y}_{rcs}\dot{\varphi}_{rcs}) \\ &+ \omega_r^2\hat{y}_{rcs}]\mathrm{e}^{\mathrm{j}\varphi_{rcs}} = K_n\hat{u}_{rcs}\mathrm{e}^{\mathrm{j}(\varphi_{vco}+\Delta\phi_{rcs})}. \end{aligned} \tag{3.21}$$

From (3.5) we have that $\Delta\varphi = \varphi_{rcs}(t) - \varphi_{vco}(t) - \Delta\phi_{rcs}$. Hence, we can properly introduce $\Delta\varphi$ in (3.21) dividing both sides of the equation by $\mathrm{e}^{\mathrm{j}(\varphi_{vco}+\Delta\phi_{rcs})}$. By knowing that $\mathrm{e}^{\mathrm{j}\Delta\varphi} = \cos(\Delta\varphi) + \mathrm{j}\,\sin(\Delta\varphi)$, and making the following substitutions:

$$\begin{aligned} &x_1 = \hat{y}_{rcs},\ \ x_2 = \Delta\varphi,\ \ x_3 = \dot{\hat{y}}_{rcs},\ \ x_4 = \dot{\Delta\varphi},\ \ x_5 = y_{pdq},\ \ x_6 = y_{pdi}, \\ &u_1 = K_n\hat{u_{rcs}},\ \ u_2 = \omega_{vco}, \end{aligned} \tag{3.22}$$

we have

$$(A + \mathrm{j}B)(\cos x_2 + \mathrm{j}\sin x_2) = u_1, \tag{3.23}$$

where

$$\begin{aligned} A &= \dot{x}_3 - x_1(x_4 + u_2)^2 + 2\xi\omega_n x_3 + \omega_n^2 x_1, \\ B &= x_1(\dot{x}_4 + \dot{u}_2) + 2x_3(x_4 + u_2) + 2\xi\omega_n x_1(x_4 + u_2). \end{aligned} \tag{3.24}$$

Separating (3.23) into real and imaginary parts, it follows that

$$A\cos x_2 - B\sin x_2 = u_1, \tag{3.25}$$
$$A\sin x_2 + B\cos x_2 = 0. \tag{3.26}$$

If we multiply both sides of (3.25) by $\cos x_2$, and both sides of (3.26) by $\sin x_2$, after solving the system we have $A = u_1 \cos x_2$ and $B = -u_1 \sin x_2$. Substituting A and B into (3.24), we can finally represent the open loop system dynamics as a nonlinear and autonomous system $\dot{\mathbf{x}} = \mathbf{F}(\mathbf{x}) + \mathbf{G}(\mathbf{u})$, with the following state space description

$$\dot{x}_1 = x_3, \tag{3.27a}$$
$$\dot{x}_2 = x_4, \tag{3.27b}$$
$$\dot{x}_3 = u_1 \cos\, x_2 - 2\xi\omega_r x_3 + x_1((u_2 + x_4)^2 - \omega_r^2), \tag{3.27c}$$
$$\dot{x}_4 = -\frac{u_1}{x_1} \sin\, x_2 - 2\left(\xi\omega_r + \frac{x_3}{x_1}\right)(u_2 + x_4), \tag{3.27d}$$
$$\dot{x}_5 = \omega_g[K_{pdq}\, x_1(-x_2 - \Delta\phi_{rcs} + \Delta\phi_q) - x_5], \tag{3.27e}$$
$$\dot{x}_6 = \omega_g[K_{pdi}\, x_1(x_2 + \Delta\phi_{rcs} - \Delta\phi_i + \pi/2) - x_6], \tag{3.27f}$$

where $K_{pdq} = K_q \hat{u}_{pdq}/2$ and $K_{pdi} = \hat{u}_{pdi}/2$ are constant values. Note that for open loop analysis, if we keep ω_{vco} as a constant excitation value, $\dot{u}_2 = 0$.

3.4 CLOSED LOOP DESCRIPTION

3.4.1 Nonlinear Representation

Although the control system is digitally implemented, we will assume only continuous signals for the closed loop modeling, once the discrete analysis will be considered later.

In order to simplify the analysis a PI controller is used, since in practice the derivative action is not implemented to avoid issues regarding the time-discrete differentiation. Furthermore, this is the most common and widely employed controller, given its robustness and easy implementation. Besides, this structure is well suited in this PLL based system. A complete analysis considering a PID controller is explored in Appendix B.

Consider the following PI control law:

$$y_c(t) = K_p\,\varphi_e(t) + K_i \int_0^t \varphi_e(\tau) d\tau, \tag{3.28}$$

where K_p and K_i are the proportional and integral gains, respectively.

According to (3.22), and substituting (3.28) in (3.3), the first and second derivative of u_2 are expressed as

$$u_2 = \omega_c + K_{vco}\left(K_p\,\varphi_e + K_i \int_0^t \varphi_e(\tau)\, d\tau\right), \tag{3.29}$$

$$\dot{u}_2 = K_{vco}(K_p\,\dot{\varphi}_e + K_i\,\varphi_e). \tag{3.30}$$

Knowing that $\varphi_e(t) = \phi_r - \varphi(t)$, and on account with (3.16), the first derivative of the phase error φ_e must consider that atan2 is a function of two variables and, as consequence, it has two partial derivatives. Hence, the first total differential are formulated as

$$\dot{\varphi}_e = \frac{y_{pdq}\dot{y}_{pdi} - y_{pdi}\dot{y}_{pdq}}{y_{pdq}^2 + y_{pdi}^2}. \tag{3.31}$$

Rewriting (3.29)-(3.31) in terms of the variables (3.22) and inserting them into (3.27), we can describe the closed loop system by choosing two additional states

$$x_7 = \varphi_e, \quad x_8 = \int_0^t \varphi_e(\tau) d\tau. \tag{3.32}$$

Finally, the state space representation of the whole nonlinear system dynamics is described as

$$
\begin{aligned}
\dot{x}_1 &= x_3 \\
\dot{x}_2 &= x_4 \\
\dot{x}_3 &= u_1 \cos x_2 - 2\xi\omega_r x_3 + x_1((\omega_c + K_{vco}(K_p x_7 + K_i x_8) + x_4)^2 - \omega_r^2) \\
\dot{x}_4 &= -\frac{u_1}{x_1}\sin x_2 - 2\left(\xi\omega_r + \frac{x_3}{x_1}\right)(\omega_c + K_{vco}(K_p x_7 + K_i x_8)) \\
&- K_{vco}\left[\frac{K_p\omega_g x_1}{x_5^2 + x_6^2}\left(K_{pdi}(x_2 + \Delta\phi_{rcs} - \Delta\phi_i + \pi/2)x_5 - K_{pdq}(-x_2\right.\right. \\
&\left.\left. -\Delta\phi_{rcs} + \Delta\phi_q)x_6\right)\right] + K_i x_7 \\
\dot{x}_5 &= \omega_g[K_{pdq}\, x_1(-x_2 - \Delta\phi_{rcs} + \Delta\phi_q) - x_5] \\
\dot{x}_6 &= \omega_g[K_{pdi}\, x_1(x_2 + \Delta\phi_{rcs} - \Delta\phi_i + \pi/2) - x_6] \\
\dot{x}_7 &= \frac{\omega_g x_1}{x_5^2 + x_6^2}\left[K_{pdi}(x_2 + \Delta\phi_{rcs} - \Delta\phi_i + \pi/2)\, x_5 - K_{pdq}(-x_2 - \Delta\phi_{rcs}\right. \\
&\left. +\Delta\phi_q)\, x_6\right] \\
\dot{x}_8 &= \phi_r - \text{atan2}(x_5, x_6),
\end{aligned}
\tag{3.33}
$$

3.4.2 Linear Representation

The description of the open loop system dynamics, as declared in (3.27), can be linearized around an equilibrium point in order to apply a linear control system design. When the system is at resonance, $\varphi_{vco} = \omega_r t$, $\Delta\varphi = -\pi/2$, and the equilibrium points $\bar{x}_n$ are obtained by considering $\dot{\mathbf{x}} = 0$ in (3.27), as follows

$$
\begin{aligned}
\bar{x_1} &= \frac{u_1}{2\xi\omega_r^2} \\
\bar{x_2} &= -\frac{\pi}{2} \\
\bar{x_3} &= 0 \\
\bar{x_4} &= 0 \\
\bar{x_5} &= \frac{K_{pdq}u_1(\pi/2 - \Delta\phi_{rcs} + \Delta\phi_q)}{2\xi\omega_r^2} \\
\bar{x_6} &= \frac{K_{pdi}u_1(\Delta\phi_{rcs} - \Delta\phi_i)}{2\xi\omega_r^2}.
\end{aligned}
\tag{3.34}
$$

According to [42], the first-order perturbation theory can be employed for the linearization of the RCS states (3.27a)-(3.27d), considering a small perturbation $\epsilon\,\omega_{r,p}$ around the resonant frequency ω_r, such that

$$u_2(\epsilon, t) = \omega_r + \epsilon\,\omega_{r,p}(t), \tag{3.35}$$

where $\epsilon \ll 1$. As a result, the states will also vary by a small amount around the equilibrium points, and the phase shift follows

$$x_2(\epsilon, t) = \bar{x}_2 + \epsilon\,x_{2,p}(t). \tag{3.36}$$

Hence, the transfer function that relates the change in phase difference, $x_{2,p}$, and a small change in the excitation frequency, $\omega_{r,p}$, denoted as H_{pf}, after several considerations (see [42] for further details), can be expressed as a first order system

$$H_{pf}(s) = \frac{X_{2,p}(s)}{\Omega_{r,p}(s)} \approx \frac{1}{s + \xi\Omega_r}, \tag{3.37}$$

while the total phase shift reads

$$\Delta\Phi(s) = -\frac{\pi}{2} - H_{pf}(s)\,\Omega_{r,p}(s) = -\frac{\pi}{2} - H_{pf}(s)(\Omega_{vco}(s) - \Omega_r). \tag{3.38}$$

Once $H_{pf}(s)$ is represented in terms of phase and frequency, the remaining elements of the conventional PLL can also be described in the same way in order to obtain the closed loop linear representation.

The frequency domain description of the phase detector, considering the linear analysis exposed in section 3.2 and the low-pass filter ($H_{lp}(s)$) dynamics, is given by

$$Y_{pd}(s) = K_{pd}(\Delta\Phi(s) - \phi_r + \Delta\phi_{rcs} - \Delta\phi_{pd})H_{lp}(s), \tag{3.39}$$

From (3.28), we can obtain the controller transfer function as

$$H_c(s) = \frac{Y_c(s)}{Y_{pd}(s)} = \frac{K_p s + K_i}{s}. \tag{3.40}$$

Applying the Laplace transform to (3.2) and (3.3), the phase and the oscillating frequency representation of the VCO in frequency domain are, respectively

$$\Phi_{vco}(s) = \frac{1}{s}\left(\omega_c + K_{vco}Y_c(s)\right) \tag{3.41}$$

$$\Omega_{vco}(s) = \omega_c + K_{vco}Y_c(s). \tag{3.42}$$

From eqs. (3.37) to (3.42), we can build the linear closed loop RFTS block diagram, as illustrated in Fig. 3.6.

Figure 3.6: RFTS block diagram (linear closed loop analysis).

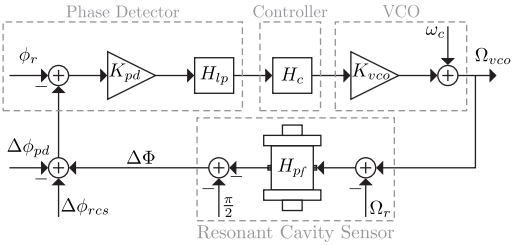

Source: The Author.

From Fig. 3.6, different input/output analysis can be performed. In this work, the main purpose is to analyze the driving frequency $\Omega_{vco}(s)$ due to a change in the RCS resonant frequency Ω_r, taking into account a constant phase shift $\epsilon_\Phi = \Delta\phi_{rcs} - \Delta\phi_{pd}$ that represents the phase delay in the RF components and cables. For this purpose, ϕ_r is kept constant to a phase reference value, while $\Omega_{vco}(s)$ is analyzed by superposition of the responses due to a specific phase input ϵ_Φ and a specific change in the resonant frequency ϵ_Ω, in a manner that $\Omega_r \to \Omega_r + \epsilon_\Omega$. Therefore, from Fig. 3.6,

$$\Delta\Phi(s) = -\tfrac{\pi}{2} - H_{pf}(s)(\Omega_{vco}(s) - (\Omega_r + \epsilon_\Omega)) \tag{3.43}$$

$$\Omega_{vco}(s) = \omega_c + K_{pd}H_{lp}(s)H_c(s)K_{vco}(\Delta\Phi(s) + \varepsilon_\Phi - \phi_r). \tag{3.44}$$

Substituting (3.43) in (3.44), we have

$$\Omega_{vco}(s) = \omega_c + K_{pd}H_{lp}(s)H_c(s)K_{vco}\left(-\frac{\pi}{2} - H_{pf}(s)(\Omega_{vco}(s) - (\Omega_r + \epsilon_\Omega)) + \epsilon_\Phi - \phi_r\right). \tag{3.45}$$

Considering $H_{ol}(s) = K_{pd}H_{lp}(s)H_c(s)K_{vco}H_{pf}(s)$ as the open loop transfer function, (3.45) can be rewritten as

$$\Omega_{vco}(s)(1 + H_{ol}(s)) = \omega_c + H_{ol}(s)(\Omega_r + \epsilon_\Omega) + K_{pd}H_{lp}(s)H_c(s)K_{vco}\left(-\frac{\pi}{2} + \epsilon_\Phi - \phi_r\right). \tag{3.46}$$

Assuming the system is initially locked at resonance, i.e. $\omega_c = \Omega_r$, and considering that $\phi_r = -\pi/2$ (sensor's phase shift in the resonant frequency), the total VCO frequency response $\Omega_{vco}(s)$ due to a fixed phase lag ϵ_Φ and a change in the resonant frequency ϵ_Ω is finally formulated as

$$\Omega_{vco}(s) = \frac{H_{ol}(s)}{1 + H_{ol}(s)}\left(\epsilon_\Omega + \frac{1}{H_{pf}(s)}\epsilon_\Phi\right). \tag{3.47}$$

The linear analysis shows that, if we assume $\phi_r = -\pi/2$, in the locked state the driving frequency $\Omega_{vco}(s)$ will present a small offset from the actual resonant frequency of the sensor, due to the system phase delay ϵ_Φ.

3.5 CONTROL ANALYSIS

For control design purposes, the block diagram exposed in Fig. 3.6 can be redesigned as the simplified block diagram depicted in Fig. 3.7(a), where $G_c(s) = H_c(s)$ and $G_p(s) = K_{pd}K_{vco}H_{lp}(s)$ represent the controller and plant transfer functions, respectively. In summary, we wish to analyze the $\Omega_{vco}(s)$ response due to a step change ϵ_Ω in the resonant frequency Ω_r in such a way that $\Omega_r \to \Omega_r + \epsilon_\Omega$. From a control point of view, we can assume the system has no phase delays, i.e. $\epsilon_\Phi = 0$, and the driving frequency is initially at the resonant frequency $\Omega_{vco}(s) = \Omega_r$. Hence, we can evaluate the control system as a classic block diagram illustrated in Fig. 3.7(b), where

Figure 3.7: Simplified RFTS block diagram (linear closed loop analysis).

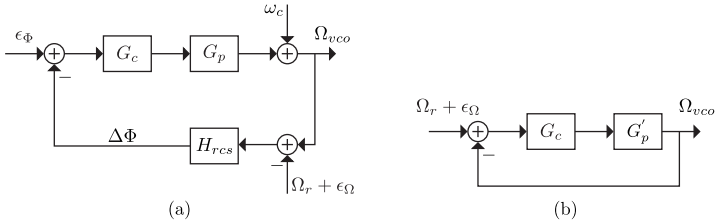

Source: The Author.

$$G_p^{'}(s) = \frac{K_{pd}K_{vco}\omega_g}{s^2 + (\omega_g + \xi\Omega_r)s + \omega_g\xi\Omega_r}. \tag{3.48}$$

Since $G_p^{'}$ is a second order transfer function of type 0, it only needs an integrator in the forward path in order to assure a zero steady state error for a step input, which is properly enhanced with a PI controller. For this reason, and also to avoid issues regarding the time-discrete differentiation, a PI controller is chosen, being

$$G_c(s) = K_p\left(\frac{s + K_i/K_p}{s}\right). \tag{3.49}$$

Therefore, the closed loop transfer function is given by

$$T_{cl}(s) = \frac{K_{pd}K_{vco}K_p\omega_g(s + K_i/K_p)}{s^3 + (\omega_g + \xi\Omega_r)s^2 + \omega_g(\xi\Omega_r + K_pK_{pd}K_{vco})s + K_iK_{pd}K_{vco}\omega_g}. \tag{3.50}$$

Applying the Routh-Hurwitz stability criterion the proportional limit gain for stability is defined as $K_p > (K_{pd}K_{vco}K_i - \xi\Omega_r(\omega_g + \xi\Omega_r))/(K_{pd}K_{vco}(\omega_g + \xi\Omega_r))$. The system has an infinite gain margin, and classical control techniques can be used for the control design implementation. Once the controller is digitally implemented, a discrete version of (3.49) is needed. Using the Euler Forward discretization method, the controller transfer function in z-domain is

$$G(z) = \frac{K_pz + (K_iT - K_p)}{z - 1}, \tag{3.51}$$

where T is the sampling time. The sampling time is chosen considering the range $0.15/\omega_{\Phi_M}$ to $0.5/\omega_{\Phi_M}$, where ω_{Φ_M} is the zero dB frequency (rad/s) of the magnitude frequency response curve for the cascaded controller and plant transfer functions [43]. The digital version of the block diagram in Fig. 3.7(a) is shown in Fig. 3.8, where the computer is represented with a sampler and a zero-order hold (ZOH).

Figure 3.8: Discrete version of the simplified RFTS block diagram depicted in Fig. 3.7(a).

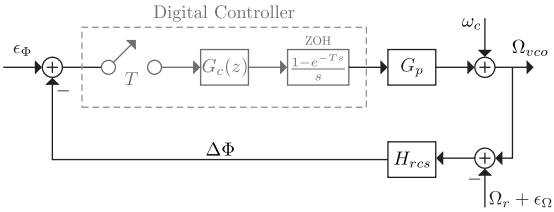

Source: The Author.

3.6 SYSTEM VALIDATION

3.6.1 Setup Implementation

A picture of the implemented RFTS using a dedicated RF circuit with off-the-shelf components is shown in Fig. 3.9. It consists of five passive devices: two power splitters (PS1 and PS2), two mixers (MIX1 and MIX2), and a hybrid port (HYB), besides two active devices: a voltage controlled oscillator (VCO) and a power amplifier (PA). The devices are connected using 50 Ω RF cables and SMA adapters. The RF components are also internally matched to 50 Ω. The control system is digitally implemented with the data acquisition board myDAQ.

The data acquisition board myDAQ has two analog inputs and two analog outputs, that can be configured to receive and provide voltage signals from -10 V to +10 V, with an A/D and D/A resolution of 16 bits, and a maximum sample rate of 200 KS/s. The VCO operates between 160 MHz and 360 MHz with a typical output power of 7.5 dBm, and a typical sensitivity tunning between 9 MHz/V and 18 MHz/V (control voltage range from 0.5 V to 18 V); PA is a monolithic amplifier, unconditionally stable, and operates between DC to 4000 MHz, with

Figure 3.9: RFTS circuit setup.

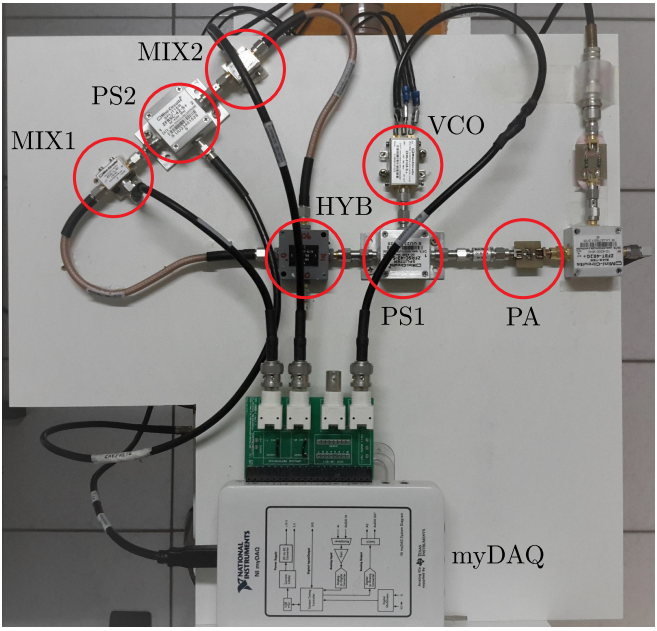

Source: The Author.

a typical gain of 19.5 dB until the frequency of 1000 MHz; MIX1 and MIX2 are based on diodes operating between 2 MHz and 500 MHz, and presenting an average conversion loss of 5.2 dB with a minimum LO power of 3 dBm; PS is a resistive device operating between DC to 4200 MHz with a typical loss of 6 dB in each port; HYB is a 90 degree hybrid octave four port based on lumped elements operating between 100 MHz to 1000 MHz with a typical insertion loss of 1.7 dB. The PA is biased using a BIAS-T and both active devices (PA and VCO) are powered by an external DC power supply. These are the main technical characteristics of the system components. All the components are addressed in Table 3.2, where their datasheet may be consulted for further information. The experimental measurements were handled in the lab with a constant room temperature of 20 Celsius degrees.

Table 3.2: List of the system components.

Component	**Company**	**Datasheet**
VCO	Minicircuits	ZX95-310A+
PA	Minicircuits	ERA-5SM+
PS	Minicircuits	ZFRSC-42+
MIX	Minicircuits	ZX05-1L+
HYB	MCLI	BL-21
BIAS-T	Minicircuits	ZFBT-4R2G+
DC-BLOCK	Minicircuits	BLK-18+
SMA Adapter	Minicircuits	SM-SM50+
50 Ω Load	Minicircuits	ANNE-50+
DAQ	National Instruments	NI myDAQ

3.6.2 Resonant Cavity Sensor Analysis

For the RCS's low-frequency model validation, we assume a resonant frequency 10^7 times lower than the actual resonant frequency for the case of 100% of water fraction ($f_r = 202$ MHz). This "low frequency factor", $K_{lf} = 10^7$, was chosen based on the experimental MUT permittivity dynamics. In Fig. 3.10 is shown the frequency response comparison between (2.11) and (3.7), where the frequency in the x-axis (in logarithmic scale) is normalized to the resonant frequency ω_r, and $K_n = 11.7$ is empirically determined. We can observe that both results present the same damping coefficient ξ. The magnitude of the high-frequency model has a zero DC gain due to the zero in the transfer function (2.11), resulting in a slightly difference from the low-frequency model magnitude in the frequency range far from the resonant frequency. The zero in (2.11) also produces a 90° phase difference between both models. This phase difference has no effect in the modeling, since the only consequence is a new phase value in the resonant frequency ($-\pi/2$ in this case). Note that both models are well correlated in the frequency operation range.

3.6.3 System Coefficients Determination

Once the RCS low-frequency model was validated, a VCO frequency sweep from 150 MHz to 290 MHz was configured. The model

Figure 3.10: Frequency response analysis for the Low Frequency RCS model validation.

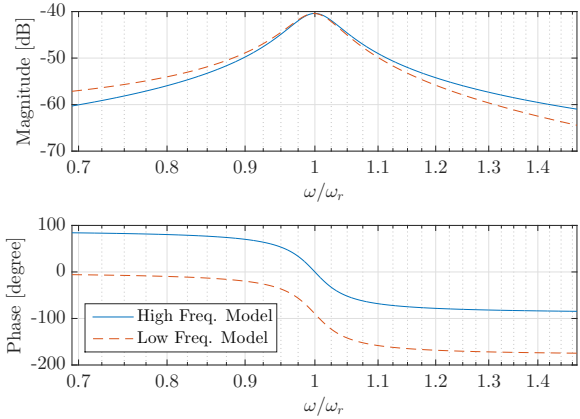

Source: The Author.

coefficients were determined by comparing the experimental results for the 100% water fraction case ($f_r = 202$ MHz) with the simulation implemented on Matlab Simulink using the block diagram exposed in Fig. 3.5. A frequency sweep from 150 MHz/K_{lf} to 290 MHz/K_{lf}, with f_r=202 MHz/K_{lf}, was configured for the model simulation. The following coefficients values were empirically determined: $\hat{u}_{pdq} = 1$, $\hat{u}_{pdi} = 1.6$, $\hat{u}_{rcs} = 18.7$, $\Delta\phi_q = -30°$, $\Delta\phi_i = -10°$, $\Delta\phi_{rcs} = 0°$.

Figs. 3.11 and 3.12 show the comparison results for *quadrature* y_{pdq} and *in-phase* y_{pdi} signals, respectively. The results show good correlation near the resonance, although it reduces before and after the resonance for both cases. This is a consequence of the impedance matching networks (not considered in the RCS dynamics), once they attenuate the transmission signal below and after the resonant frequency. This behaviour can be noticed from the magnitude graph exposed in Fig. 3.13, in which the experimental curve presents a higher quality factor. Another detail about the real system is that the magnitude and phase of the transmission coefficient of passive devices and RF cables, also vary according to the excitation frequency, which contributes to the differences between the simulated and experimental results. Furthermore, the VCO output power is not constant in all frequency range. Finally, in Fig. 3.14 we can see the difference in the phase response, since the experimental curve presents the phase contribution of the additional

poles and zeros from the impedance matching networks. In the linear region, around the resonance, the experimental curve slope is also slightly different from the simulation. Although this difference influences the phase detector gain, as it will be clear in the next session, the model coefficients are empirically determined in order to overcome this discrepancy.

Figure 3.11: Comparison between experimental (Exp.) and simulated (Sim.) results for *quadrature* y_{pdq} signal in the open loop analysis.

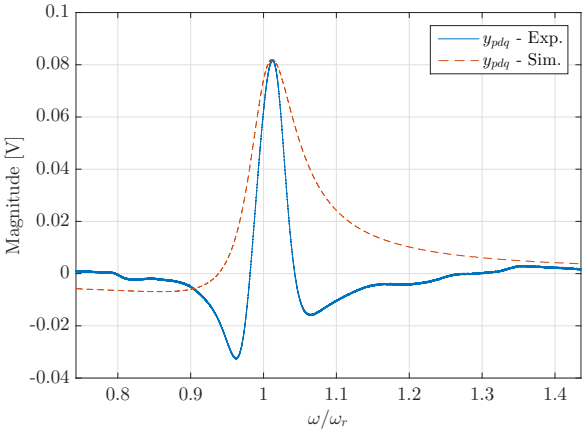

Source: The Author.

Figure 3.12: Comparison between experimental (Exp.) and simulated (Sim.) results for *in-phase* y_{pdi} signal in the open loop analysis.

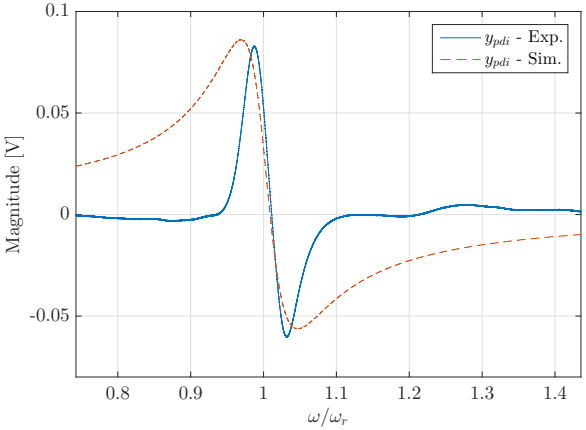

Source: The Author.

Figure 3.13: Comparison between experimental (Exp.) and simulated (Sim.) results for the magnitude M response in the open loop analysis.

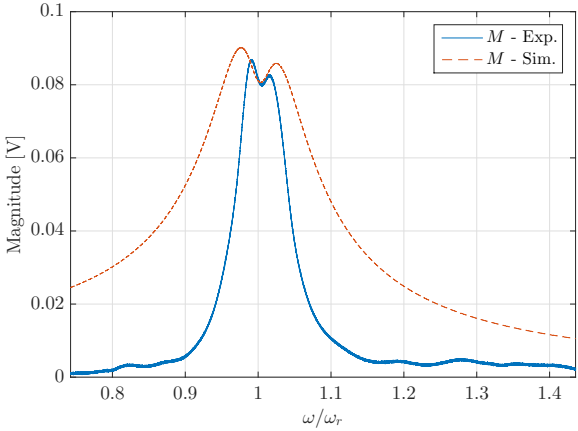

Source: The Author.

Figure 3.14: Comparison between experimental (Exp.) and simulated (Sim.) results for the phase φ response in the open loop analysis.

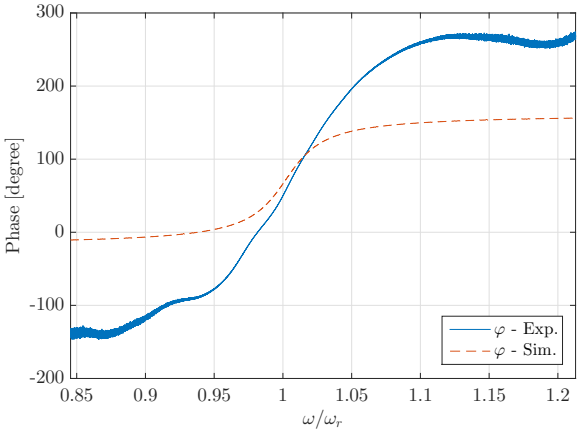

Source: The Author.

3.6.4 Resonant Frequency Tracking System Analysis

For the RFTS validation, the nonlinear and linearized system representations, formulated in (3.33) and (3.47), respectively, were simulated and compared with experimental measurements. For the simulations, the VCO gain $K_{vco} = 10 \times (2\pi 15 \times 10^6)/K_{lf}$ [rad/sV] was set based on the actual average VCO sensitivity (15 MHz/V), while the PD gain $K_{pd} = 1.6$ (present in the linear model), the phase delay $\Delta\phi_{pd} = -10.2°$, and the constant $K_q = 0.7657$ were empirically defined.

Three different projects, based on the linearized system depicted in Fig. 3.7(b), were implemented using the root locus technique. The PI gains were chosen taking into account distinct performance characteristics, such as the settling time t_s (within $\pm 2\%$ of the steady-state value), and the overshoot percentage $\%OS$. The main parameters of each control project are summarized in Table 3.3, where t_s and $\%OS$ are the calculated parameters, while $t_s^{'}$ and $\%OS^{'}$ are the simulated results. Fig. 3.15 shows the system response to a unit step input in time-domain for each project. Project 01 presents the greater overshoot and settling time. On the other hand, Project 02 presents less overshoot and a shorter settling time, when compared with Project 01. Finally, Project 03 presents the shorter settling time and no overshoot. According to Table 3.3, the simulation results from Project 03 have better convergence to the calculated parameters than the first and second projects, once the third pole of the closed loop transfer function (3.50) is practically canceled by the compensator zero. Hence, Project 03 can be approximate to a second order system, which is considered for theoretical calculus of design parameters t_s and $\%OS$. Difference equations were implemented by inspecting (3.51) using a C# application, and the sampling time for each project was selected following the methodology described in Section 3.5.

Table 3.3: Simulation results for the implemented controller projects

	K_p	K_i	t_s [s]	$t_s^{'}$ [s]	$\%OS$	$\%OS^{'}$	Compensator zero [rad/s]	Third pole [rad/s]
Project 01	0.1	0.15	9	9	27	37	-1.5	-4.22
Project 02	0.1	0.05	7	7.5	1.1	10.1	-0.5	-3.9
Project 03	0.2	0.05	1.61	1.63	0.24	0.24	-0.25	-0.249

A phase reference value of $\phi_r = \pi/2$ is set for the system tracking, which is a value corresponding to a locked frequency near to the resonance (see Fig. 3.14). The RFTS is initially locked (with an offset) at the

Figure 3.15: System responses to a unit step input according to different control projects, considering the simplified system presented in Fig. 3.7(b).

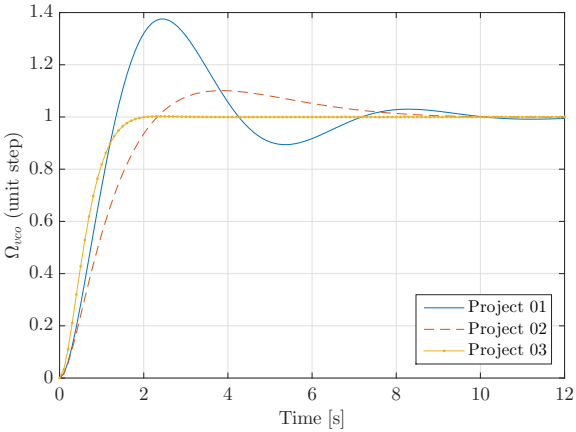

Source: The Author.

resonant frequency corresponding to 90% of water fraction ($\Omega_r = 205.8$ MHz). In order to emulate a step change in the water fraction inside the sensor's pipe, a portion of water corresponding to a step change of $\epsilon_\Omega = 1$ MHz in the resonant frequency Ω_r is manually added to the sensor's pipe.

Figs. 3.16, 3.17 and 3.18, show the comparison of experimental and simulated results from the nonlinear (3.33) and linearized (3.47) system responses, considering the three control projects. The nonlinear system is well followed by the linearized solution for all cases, demonstrating the reasonable usage of the linearized system for the controller design. The experimental results are also in agreement with the simulations, specially for the second (see Fig. 3.17) and third (see Fig. 3.18) projects. There is a slightly difference between the experimental and simulation results for the first project (see Fig. 3.16), however the overshoot percentage is well correlated to the simulation results, assuring the fidelity of the system coefficients determination. In fact, the semi-empirical approach employed in the system modeling, besides all the considerations exposed in the previous sections, certainly are error sources that explain in part the differences between simulated and experimental results. Furthermore, the correct choice of sampling time is determinant for the convergence of the results. In Project 01, a sampling time $T = 283$ ms is set, while for Project 02 $T = 200$ ms, and Project 03 $T = 106$ ms. These performance

Figure 3.16: Comparison between simulated (nonlinear and linearized solutions) and experimental results for the RFTS validation employing the controller designed in Project 01.

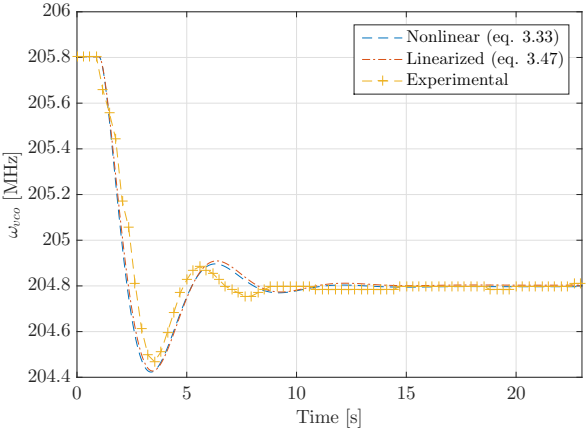

Source: The Author.

characteristics are well suitable for both applications addressed in this thesis, specially for the second one, where the dynamics of the fat content variation in the milk production is quite slow, occurring within a period between 10 to 15 seconds.

Figure 3.17: Comparison between simulated (nonlinear and linearized solutions) and experimental results for the RFTS validation employing the controller designed in Project 02.

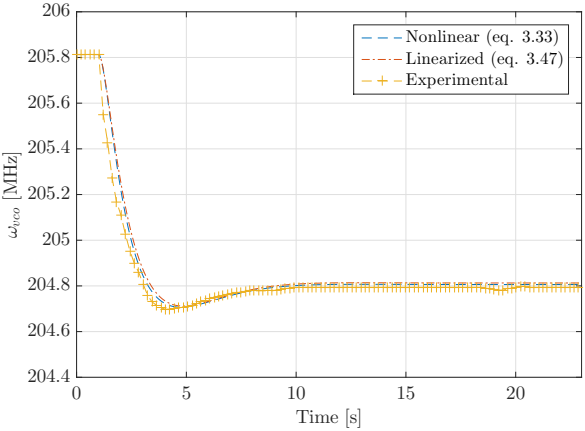

Source: The Author.

Figure 3.18: Comparison between simulated (nonlinear and linearized solutions) and experimental results for the RFTS validation employing the controller designed in Project 03.

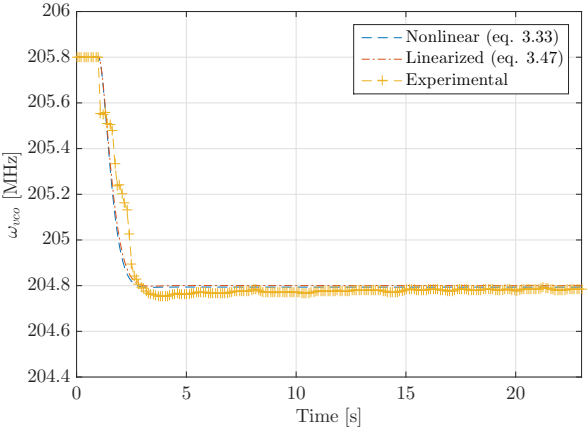

Source: The Author.

3.7 SUMMARY

The Resonant Cavity Sensor as part of a measurement system has been used in many applications. The phase and/or amplitude information can be used for relating the resonant frequency to the desired measurement parameter. For this purpose, different external circuit approaches have been published in the literature to track the resonant frequency, and one of the most efficient is the usage of a PLL based architecture, since it is well suited in a large number of applications. In this approach, the phase detector play an important role in the system response, and the quadrature implementation has proven to be an attractive choice, since both magnitude and phase information can be acquired, increasing the degree of freedom of the system.

In view of accurately design the system controller, the correct modeling of the whole system is mandatory. In this chapter, we have presented the semi-empirical modeling and control design of a PLL based RFTS applied to the resonant cavity sensor explored in Chapter 2. The model was developed by considering the physical characteristics of the elements of the system and therefore, can be extended to others resonant based sensors. By simulation and experimental results on a water cut measurement setup, the developed model demonstrates accurate reproduction of the real application. In addition, we exemplify the use of the model for the design of a PI controller. Nonlinear analysis can also be performed using new control strategies, once the system proved to be well described and verified. Three projects with three different set of specifications were implemented in order to analyze the measurement system performance. Once the experimental results presented high correlation with the simulations we can conclude that the modeling is well consistent.

The uses and applications of the model are a design and operation tool for RFTS systems, simulation framework, or a useful tool for analysis and design of advanced control strategies to the optimal operation of the system. Further research should include the design and comparative study of the closed-loop system performance with optimal and model based predictive control techniques, robust control, and adaptive control methodologies. In particular, adaptive control strategies are of great interest in this system due to its parameters variation.

4 INDUSTRIAL APPLICATIONS

The applications reported in this Chapter have been published previously in [44] and [16]. All the experimental measurements were performed using the first version of the RFTS described in Chapter 3.

4.1 WATER FRACTION DETERMINATION IN STRATIFIED (WATER/GAS) FLOW PATTERN

4.1.1 Introduction

Two-phase flows, such as liquid-liquid and gas-liquid, are very common in the oil and gas industry. The flow pattern of these regimes is determined by a large number of variables, for instance, the fraction and velocities of each phase, as well as its physical properties, the geometry and the characteristics of the pipe, i.e., diameter, shape, inclination, and roughness [45]. Stratified water-gas and water-oil flows are frequently found in horizontal pipelines [46], [47]. Regarding the first, according to [46], as the superficial gas velocity increases the flow becomes wavy, and in high void fraction the resulting flow regime will have an annular characteristic. When both, superficial gas and superficial water velocities increase, the flow alter to intermittent leading to slugs or elongated bubbles. As the superficial water velocity still increasing a water continuous flow pattern with dispersed bubbles will take place. Fig. 4.1 illustrates the flow regime map for a horizontal pipe, considering the water and gas superficial velocities.

Among the water-oil flows, the flow regime map has characteristics quite similar to the water-gas flows, as we can see in Fig. 4.2. According to [48], for low water and oil superficial velocities there are segregated flow regimes defined as Stratified flow (ST) and stratified with some mixing at the interface (ST&MI). As the oil and water superficial velocities increase the flow pattern assumes a dispersed characteristic. If the water superficial velocity increases, the oil changes into dispersed bubbles in water over a water layer (DO/W&W), and as the water turns into the dominant phase, an emulsion of oil in water (O/W) emerges. On the other hand, if the oil superficial velocity increases, the dispersion of water in oil (DW/O) and oil in water (DO/W) coexist and an emulsion

Figure 4.1: Flow regime map for water-gas flows in a horizontal pipe.

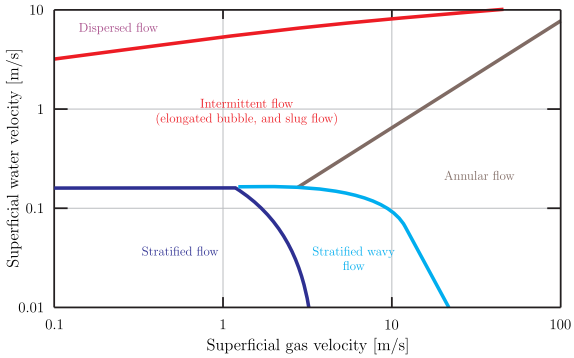

Source: Adapted from [46].

Figure 4.2: Flow regime map for water-oil flows in a horizontal pipe.

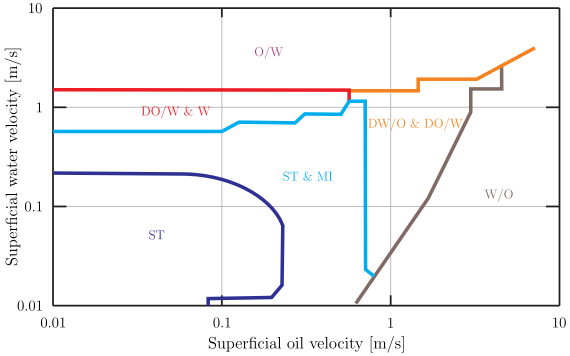

Source: Adapted from [48].

of water in oil (W/O) takes place when the oil becomes the dominant phase.

As we can observe from Figs. 4.1 and 4.2, stratified flows are present in many regions of the flow map. Although these flow maps are very dependent of some variables, such as the inclination and the diameter of the pipeline [46], [48], [49], in general at low superficial velocities, segregated flows are always found [50]. For this reason, it is appropriated to investigate the application of the RCS as a water cut meter in water-gas stratified regime. In the next sections we will discuss the experimental results obtained with this application.

4.1.2 Setup implementation

Fig. 4.3 shows a photograph of the measurement setup implemented. In Fig. 4.3(a) and 4.3(b) we can see the RF circuit coupled to the sensor as well as the identification of each component, respectively. In Fig. 4.3(c) we can observe the whole setup with the impedance matching network, that was designed for the case of 100% [19], coupled to the RCS. For the real time measurement and data analysis we developed a graphic user interface using Microsoft Visual Studio.

Figure 4.3: Measurement setup. (a) RF circuit coupled to the RCS. (b) Identification of the RF components in the circuit. (c) The whole setup (the RCS and the impedance matching network coupled to it in detail).

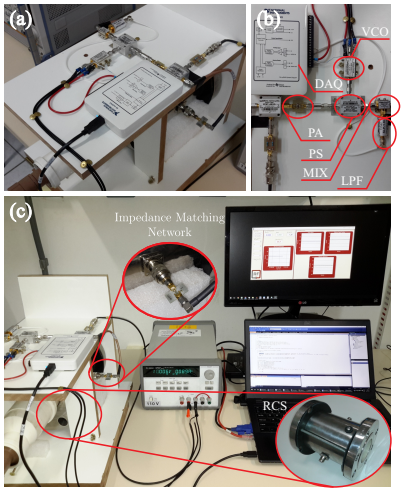

Source: The Author.

The measurements were performed taking into account a water-air stratified flow pattern as shown in Fig. 4.4.

4.1.3 Results and discussion

Firstly, the system was evaluated in open loop, varying the VCO control voltage from 0 V to 10 V, and the phase detector response was observed for the cases from 0% to 100% of water fraction (W_f) with a step of 10%. The phase detector response for each case can be seen in

Figure 4.4: Water-air stratified flow pattern.

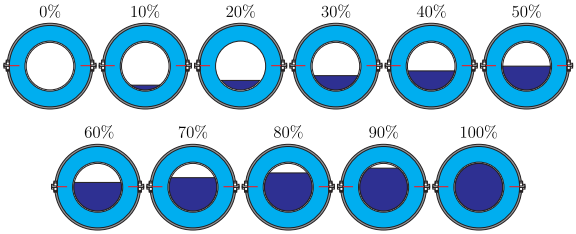

Source: The Author.

Fig. 4.5.

As a consequence of the nonlinear behavior of the phase detector response, which is based on the cosine of φ_{er}, the maximum value of y_{pd} occurs at the resonant frequency, when $\varphi_{er} = 0$ (see Fig. 4.6). As we can observe from Fig. 4.5, the magnitude of the signal decreases as the water fraction decreases, and at the same time the resonant frequency increases. The phase error curves for each percentage of water fraction are shown in Fig. 4.6. In Fig. 4.7 is shown the curve containing the maximum values of y_{pd} for each percentage of water fraction. According to Fig. 4.7, the maximum value for the case of 0% is around 7 mV. Therefore, the controller was set for tracking a reference voltage of $y_r = 5$ mV. With this approach, we can notice that the system tracks the resonant frequency with a variable offset from the actually value. At low water fraction the locked frequency is closer to the actual resonant frequency than at high water fractions.

For the validation of the system we performed (i) several step changes of the water fraction and (ii) a continuous linear variation of the water fraction inside the pipe of the sensor.

In the first case, the pipe of the sensor was initially empty and we added samples of water corresponding to 10% of water fraction (210 ml) with a beaker scale. The VCO frequency ω_{vco} is shown in Fig. 4.8. The main reason for the oscillatory response in Fig. 4.8 is due to the turbulence caused in the water after the water samples being put into the sensor's pipe. Fig. 4.9 displays the VCO frequency curve (in ω_{vco}, Water-fraction)-plane considering a reference tracking value $y_r = 5$ mV. This curve was identified and approximated by a fourth degree polynomial equation. A mean water fraction sensitivity of $0.17\%/W_f$ is achieved with a VCO frequency ω_{vco} around 203 MHz.

In the second case, the sensor's pipe is initially filled with 100% ($\omega_{vco} \approx 197.5$ MHz) of water. The content of water is drained until 80%

($\omega_{vco} \approx 199.4$ MHz), and then until 60% ($\omega_{vco} \approx 201.5$ MHz) as shown in Fig. 4.10. The results show that the automatic system allows the sensor to measure in a full range (0% to 100%) of water fraction. Although the measurements were done using water/air mixtures, analogous results can be obtained using water/oil mixtures, since the relative permittivities of air and oil have similar values, as stated in [51].

4.1.4 Conclusions

In this application was investigated the feasibility to infer the water fraction in a stratified water-gas flow regime using the first version of the RFTS discussed in Chapter 3. It was verified that the system was capable of measuring in a full range (0% to 100%) with a mean water fraction sensitivity around $0.17\%/W_f$. In this way, we are convinced that the resonant cavity sensor can become an autonomous instrument and with real possibilities of enhancing a commercial two-phase water-cut meter, in stratified flow pattern, for the oil and gas industry after some improvements, such as the robustness of the external circuit.

Figure 4.5: Phase detector response in stead state as a function of the VCO oscillation frequency for each percentage of water fraction.

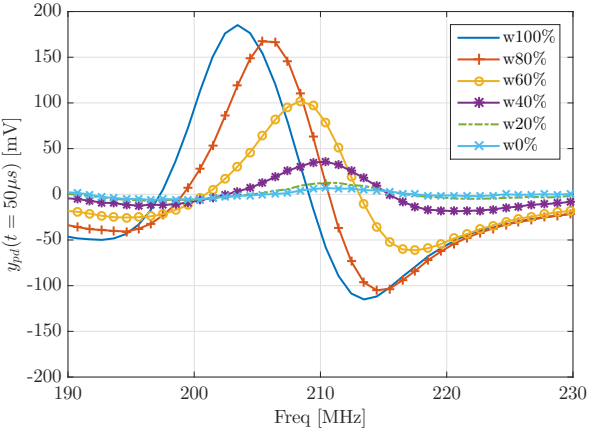

Source: The Author.

Figure 4.6: Phase error as a function of the VCO oscillation frequency for each percentage of water fraction.

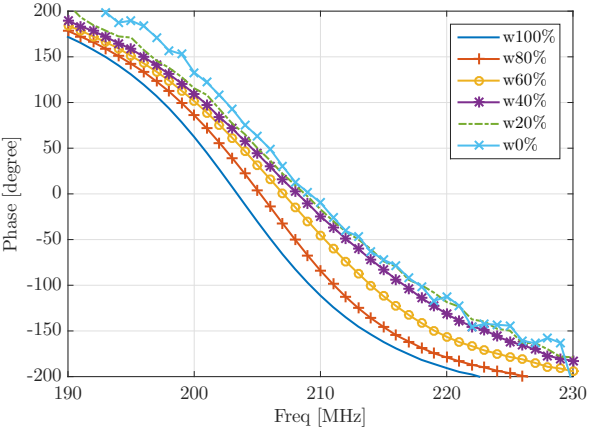

Source: The Author.

Figure 4.7: Maximum values of the phase detector response as a function of water fraction.

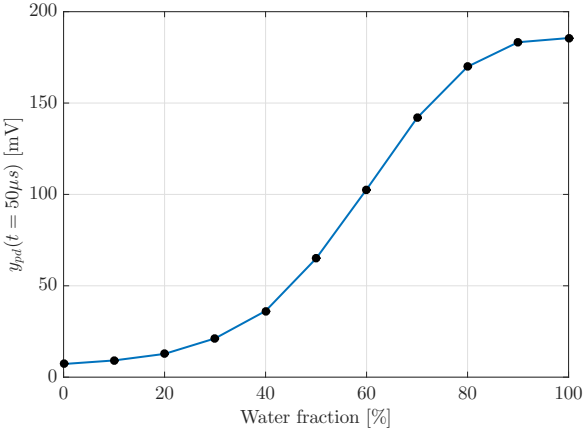

Source: The Author.

Figure 4.8: VCO frequency for a step variation between 0% to 100% of water fraction with steps of 10%.

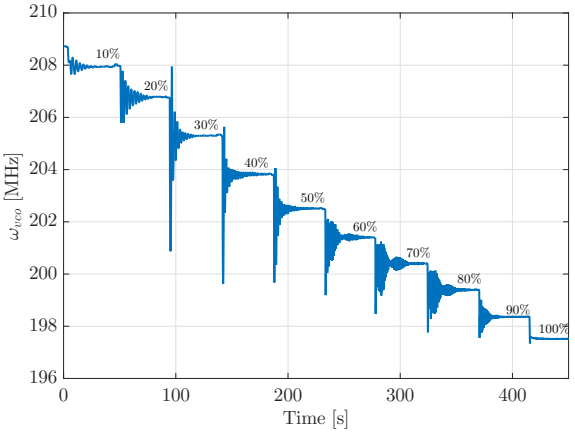

Source: The Author.

Figure 4.9: Water fraction vs ω_{vco} considering the reference tracking value $y_r = 5$ mV.

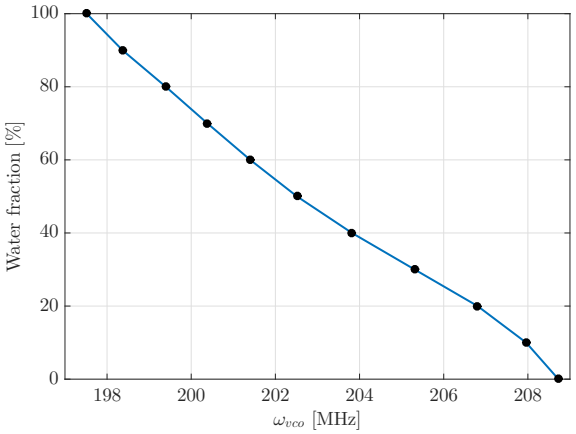

Source: The Author.

Figure 4.10: VCO frequency for a linear variation between 100% to 60% of water fraction with linear variations intervals of 20%.

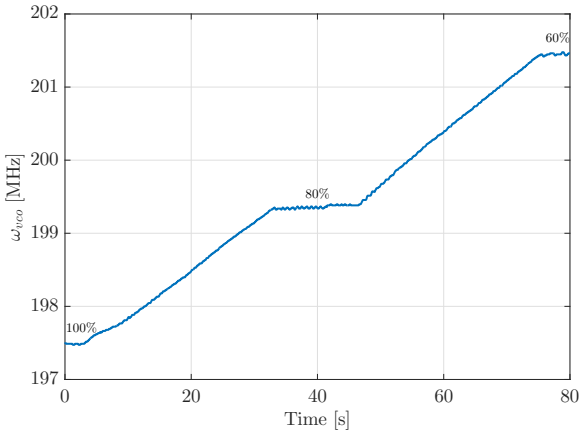

Source: The Author.

4.2 SOLIDS AND FAT CONTENTS DETERMINATION IN BOVINE MILK

Monitoring the milk quality is of fundamental importance in the food industry since milk is one of the most common product in a daily diet. The control of milk composition and detection of adulteration in raw materials are crucial to assure the quality of dairy based products. Different technologies for the monitoring of milk constituents in substitution of chemical processes have been reported. Recent studies showed that microwave sensors have a good potential for measuring the milk moisture content. In this application, we proposed the determination of total solids and fat contents using the measurement system based on resonant cavity sensor. Its main advantages comprises non-invasive and non-destructive characteristics and fast response. Additionally, the geometry of the cavity is adapted for easy deployment in industrial facilities. We used nine characterized milk samples to demonstrate the feasibility of the system. The results showed an adequate correlation between the system response and the volume fractions of total solids and fat constituents, proving that the system is a useful platform for the analysis of milk quality.

4.2.1 Introduction

Milk is one of the most common food present in daily diet of many cultures, being recommended in most dietary guidelines around the world. Furthermore, it is considered as a rich source of essential amino acids for human nutrition, and its protein may have good effects on growth and recovery from undernutrition [52], [53]. Bovine milk contributes with 85% of global production [54]. According to the most recent report of the Food and Agriculture Organization of the United Nations [55], in 2016 approximately 659.15 million tonnes of bovine milk were produced in the world. Within this scenario, Brazil is the major milk producer in Latin America and has the fifth greater average production in the world (considering the period between 1993 and 2016), with approximately 33.62 million tonnes produced in 2016 [56]. Because of the dairy sector importance in the economy as a whole, the constant monitoring of the milk quality becomes imperative in industrial manufacturing facilities for characterizing different types of milk, and also to identify possible adulteration. Additionally, it turns necessary

to keep an effective control in the selection of raw materials for the production of certain dairy products, as for example, specific types of cheeses, offering authentic products for the consumers [57].

One of the biggest obstacles in proper determination of milk quality arises from a wide diversity among various milk samples. Bovine milk is a complex multi-component liquid whose total solids, fat droplets and other components are immersed or dissolved in an aqueous background to form an intricate substance. The constituents of milk exhibit widely differing characteristic lengths, leading to wide spatial scaling [58]. The determination of milk constituents are generally made through laboratory analysis by means of different chemical processes. As reported in [59], the routine chemical approaches used are costly and time consuming, require skilled labor, suffer from large amounts of chemical reagent, demand high water consumption, and generates high waste liquid emissions.

Recently, some alternative technologies have been applied for monitoring the milk quality and detecting adulteration. In [60], a methodology based on electrical impedance measurement is presented for the detection of bovine milk adulteration, specially due to the addition of water. The developed dedicated system allows to perform in-situ measurements. Milk adulteration is also investigated using a near-infrared diffuse reflection based methodology [61], where the system response is monitored while gradually adding water to the samples, validating the feasibility of using this process in substitution of cryoscope-based laboratory tests. In [62], an optofluidic microviscometer is implemented to investigate its potential employment in milk adulteration analysis by means of adding water, flour, starch, and urea. A sensor based on microwave absorption is explored in [63] for determination of moisture content in milk. The results showed a good correlation between the total solids content of various milk samples with the normalized signal strength. The main disadvantage of this technique is the invasive way of the measurements. In [64] the feasibility of using a resonant cavity sensor (RCS) for detection of different milk compositions is studied. They used S-parameters information to estimate the fat and protein content of three different kinds of milk (whole, semi-skimmed, and skimmed). It is also observed the sensor capability for detecting spoiled milk samples. The results proved to be useful for the implementation of real-time measurement systems based on resonant cavity sensors.

All the previous sensors are well adapted for in-situ measurements, but in a laboratory scale. A complete real-time system for in-line milk quality assessment in an industrial facility is described in [65]. The

system is based on near-infrared spectroscopic sensing and it is used for monitoring various milk constituents, such as, fat, protein, and lactose contents during milking by a milking robot with good precision and accuracy. Despite the fact that this technology presents good results it can be very expensive, as stated in [64].

According to the most recent report from the Brazilian Annually Relation of Social Information (*Relação Anual de Informações Sociais, 2015*), Brazil has 3,307 establishments, including processing plants and dairy factories. Taking into account the average monthly production of the dairy industry in some states and the definition of size of industrial establishments according to the number of employees provided by [66], 90% of this amount can be considered as small-and medium-sized industries. In these industries, the fat content measurement in the standardization process is performed offline with equipments that provide the result from 60 seconds (modern technologies) to 30 minutes (ancient technologies). Huge companies as Foss, Gea and Tetrapak commercialize different solutions for the automation of the standardization process, but the main barrier for implementing automatic systems in small-and medium-sized industries concerns of high costs and specialized labor for the system maintenance, once all the existent options are imported. Within this scenario, the development of national technologies could provide attractive solutions for the major part of dairy industry in Brazil, improving the quality and reliability of the production. As a consequence, the quality of the products may also increase, enhancing the exportation and the national milk production chain as a whole.

In this chapter, the feasibility of using a resonant cavity sensor as part of a complete measurement system for in-line monitoring of moisture, total solids and fat contents is investigated. Nine milk samples were used in order to validate the measurements, whose physicochemical characteristics were previously analyzed following a rigorous methodology. Preliminary results show a linear stable response of the sensor with a good sensitivity, proving that the system is very promising for real-time monitoring of milk quality at industrial scale. A brief study about the implementation of an automatic standardization system, based on the in-line monitoring of the fat content using a resonant cavity sensor, is also addressed. A comparative table with the technologies mentioned above and their main characteristics is shown in Table 3.1, where we can compare the approach explored in this thesis.

Table 4.1: A comparative table of some technologies applied for milk monitoring and their main characteristics in the state of the art.

Author	Technology	Application	Main characteristics	Limitations
G. Durante et. al. (2016) [60]	Electrical impedance	Detection of milk adulteration	Various adulterants tests, low cost and low circuit complexity	Invasive method, difficult to identify the type of adulterant, laboratorial sample measurements
L. Ribeiro et. al. (2016) [61]	Near-Infrared Diffuse Reflection	Detection of milk adulteration	Water adulteration tests, maximum uncertainty less than 3%	Complex apparatus, laboratorial sample measurements
P. S. Venkateswaran et. al. (2016) [62]	Optofluidic Microviscometer	Detection of milk adulteration	Water, flour, starch and urea adulteration tests	Difficult to identify the type of adulterant, laboratorial sample measurements
D. Agranovich et. al. (2016) [63]	Microwave absortion	Milk characterization	Well adequate for total solids monitoring	Invasive method, laboratorial sample measurements
M. Kawasaki et. al. (2008) [65]	Near-infrared spectroscopic	Milk quality monitoring	On-line measurements, well adequate for the monitoring of fat, protein and lactose constituintes in industrial facility	Complex apparatus, expensive system
K. H. Joshi, et. al. (2015) [64]	RCS	Milk quality monitoring	Detection of fat contents and spoiled milk, using the magnitude of the transmission signal	Laboratorial sample measurements using a VNA, Flow pattern dependence
This thesis	RCS	Milk characterization	Determination of total solids and fat contents in bovine milk, in-line, using a resonant frequency tracking system based on a PLL	Flow pattern dependence

4.2.2 Materials and methods

4.2.2.1 Physicochemical analysis and sample preparation

Physicochemical analyses on three different milk samples (whole - W, semi-skimmed - SS, and skimmed - S) were carried out, in triplicate, according to the methodologies described by Association of Analytical Chemistry (AOAC), using analytical grade chemicals. In order to ensure the quality of the samples, their density, acidity and pH values were determined. The milk density ($g\,cm^{-3}$) was measured with a Thermo Lacto-Densimeter (Quevenne Tip), while the titratable acidity (lactic acid g/100g), with 0.1 mol equival/L NaOH, and the pH values were measured using a pH meter (MP220, Metler-Toledo) by the potentiometric method. Additionally, the total solids and fat contents were determined. Total solids content, (g/100g), was determined from 5 g samples by drying to constant weight at 105 °C, while fat content, (g/100g), was analyzed by Gerber method [67].

From the three main characterized samples (W, SS, and S) we prepared six additional (A1, A2, A3, B1, B2, and B3) by successive mixing. A test tube was used for measuring the contents of each sample to fill the total available volume inside the RCS (2000 mL). The temperature of each sample was measured with a mercury thermometer before each measurement. Table 4.2 lists the monitored temperatures and resultant compositions of each sample. The physicochemical composition of the last six samples were calculated by mass balance.

The obtained physicochemical data was expressed in terms of mean and standard deviation. It was possible to note that for all milk samples probed the density, titratable acidity and pH values (Table 4.3) are in accordance with the official regulation established in Brazil [68]. Likewise, the total solids and fat contents are in consonance with the Brazilian Normative Instruction No. 62 [68], that establishes minimal values of 8.40 g/100g and 0.00 g/100g, respectively.

4.2.2.2 Measurement system setup

All measurements were done in a single day at the laboratory with a room temperature fixed at 25 °C. Fig. 4.11(a) shows the whole measurement setup consisting of the RCS connected to the RF circuit

Table 4.2: Characteristics of the samples.

Samples	**Temperature** [°C]	**Composition** [ml]
W	25	2000 W
SS	24.8	2000 SS
S	25	2000 S
A1	24.7	1000 W + 1000 SS
A2	24.5	1000 W + 1000 S
A3	24.5	1000 SS + 1000 S
B1	24.5	1000 A1 + 1000 A2
B2	24.5	1000 A1 + 1000 A3
B3	24.5	1000 A2 + 1000 A3

(detailed in Fig. 4.11(b)) and the computer with the control software. The test tube and the three main samples used for preparing the additional samples are shown in Fig. 4.11(c).

Table 4.3: Physicochemical composition of the 9 different milk samples.

Samples	**Density** [g cm^{-3}]	**Titratable acidity** [g lactic acid/ 100g]	**pH**	**Total solids** [g/100g]	**Fat** [g/100g]
W	1.031 ± 0.000	0.131 ± 0.003	6.87 ± 0.02	11.50 ± 0.25	3.20 ± 0.00
SS	1.034 ± 0.000	0.128 ± 0.003	6.86 ± 0.01	9.95 ± 0.09	1.20 ± 0.00
S	1.035 ± 0.000	0.131 ± 0.003	6.83 ± 0.02	9.04 ± 0.13	0.10 ± 0.00
A1	1.033 ± 0.000	0.131 ± 0.003	6.81 ± 0.07	10.73 ± 0.15	2.20 ± 0.00
A2	1.033 ± 0.000	0.127 ± 0.003	6.78 ± 0.01	10.27 ± 0.18	1.65 ± 0.00
A3	1.035 ± 0.000	0.126 ± 0.005	6.79 ± 0.03	9.50 ± 0.08	0.65 ± 0.00
B1	1.033 ± 0.000	0.131 ± 0.003	6.80 ± 0.00	10.50 ± 0.16	1.93 ± 0.00
B2	1.034 ± 0.000	0.127 ± 0.003	6.84 ± 0.00	10.11 ± 0.11	1.43 ± 0.00
B3	1.034 ± 0.000	0.128 ± 0.002	6.90 ± 0.01	9.88 ± 0.13	1.15 ± 0.00

Figure 4.11: (a) The whole measurement setup. (b) Detail of the RCS attached to the RF circuit. (c) The main samples (W, SS, and S) and the test tube used to obtain the additional samples.

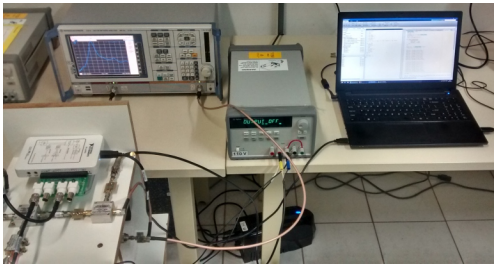

(a)

(b)

(c)

Source: The Author.

4.2.3 Results and discussion

The correlations between the VCO frequency (ω_{vco}) and the total solids and fat contents are shown in Figs. 4.12 and 4.13, respectively. As we can deduce from Fig. 4.13, ω_{vco} increases as the fat content increases. This can be explained because the real part of the permittivity decreases as the milk moisture decreases [69], consequently rising the resonant frequency of the RCS, in agreement with (2.4).

We can also observe from Fig. 4.13 that the three main samples (W, SS, and S) are disposed near to the straight line, with W and S samples in the opposite extremes of the interval, and SS near to the middle. The rest of obtained samples are all within this interval. This proves that the measurement system may be roughly linear even for a small range for both total solids ([9.95 to 11.5] g/100g) and fat ([0.1 to 3.2] g/100g) contents. The sensitivity for the total solids and fat contents are approximately [0.08 and 0.1] g/100g MHz, respectively. The discrepancies from the linear response may be explained from the standard deviation of the physicochemical composition analysis indicated in Table 4.3. An additional source of error can be related to the preparation of the six mixed samples (A1 to B3) due to the test tube scale, which was not taken into account for mass balance calculus.

Based on Pearson's correlation coefficient and the p-values with 95% confidence intervals for the coefficient estimates, the system frequency ω_{vco} is highly correlated ($P < 0.05$) with total solids and fat contents. These results allow the prediction of the concentration of total solids and fat contents by monitoring ω_{vco}.

All the information about the correlation analysis are summarized in Table 4.4.

Table 4.4: Correlation analysis: milk constituents against ω_{vco} [MHz].

Constituent	**Pearson's coefficient**	**p-value**	**Sensitivity** [g/100g MHz]	**y-intercept** [MHz]	R^2
Total solids	0.960	<0.001	0.0791	196.181	0.9228
Fat	0.958	<0.001	0.0997	197.963	0.9189

Figure 4.12: Correlation between total solids content and the VCO frequency ω_{vco}.

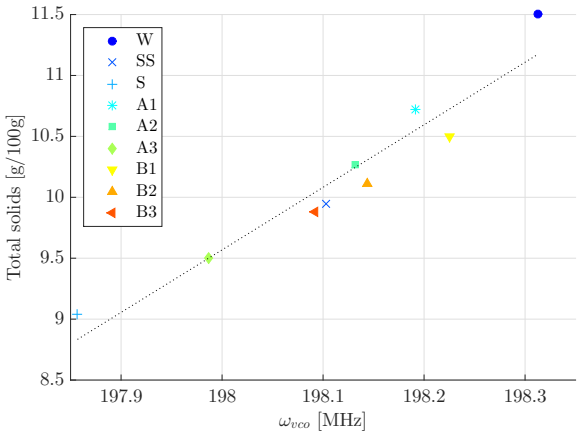

Source: The Author.

Figure 4.13: Correlation between fat content and the VCO frequency ω_{vco}.

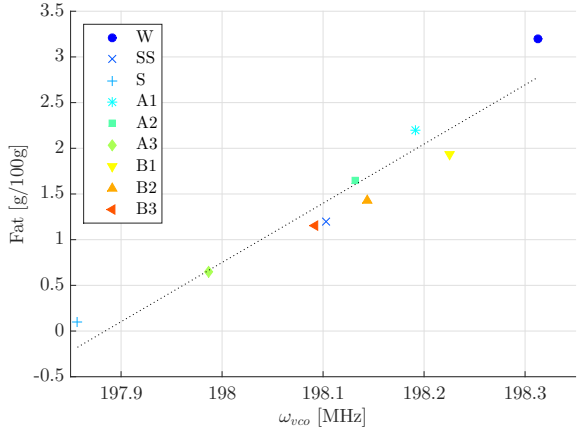

Source: The Author.

4.2.4 Propose of an Automatic Standardization System

In several industry sectors there is a need of separate a liquid in distinct components, for instance, in petroleum industry in which crude oil, containing salt water, gas and oil is separated and processed by means of different production stages. In the food industry, specifically in dairy industry, the separation of cream, a high-fat component, and the skimmed-milk, a low-fat component, is of fundamental importance for the standardization process, one of the most important stage in the milk production.

In the standardization process, raw milk from different animals is separated and then standardized to a specific fat percentage in order to produce milk and other derivatives, such as different types of cheese, cream, yogurt, among others. The variation in the fat content of raw milk is mainly due to the different bovine species, feeding of the herd and also due to distinct periods of the year.

The separation process is usually done using a separating centrifuge. The most common form of standardization is to manually adjust the centrifuge's valves so that it produces the milk with a desired percentage of fat. This method is widely used in most small and medium-sized dairy factories in Brazil. In general, samples are manually collected in line. Then, offline measurements are performed to adjust the valves as the percentage of milk fat changes. As stated before, the time wasted for measuring the fat content may vary from a minute to a half hour, depending on the equipment used. The manual control is obviously inefficient, since it cannot avoid suddenly changes in the process and is subject to a greater probability of error, given the repetitive sampling work and tests that are usually done in short periods of time, in order to achieve greater accuracy.

Different systems have been used in order to automate the standardization process. The majority of them first separates the raw milk using centrifuges, then employ different mechanisms in order to mix the cream and skimmed-milk according to the desired fat content. Among the reported mechanisms, some of them are based on physical quantities measurements, such as flow [70] and density [71], [72]. In the first system, the main disadvantage is the need of additional tanks in order to properly standardize the milk, slowing the process, besides the need of additional auxiliary equipments, such as pump and valves, that increases the costs and the frequency of maintenances. In the latter ones, the main issue is related to the accuracy of the measurements once

it depends on the reliability of the densitometers that can not provide good resolutions in the measurements. Systems with automatic sampler are reported in [73] and [74], where in the latter paper a thermal-optical approach is used. Theses systems can be considered as semi-automatic systems, once milk samples are periodically withdraw from the milk flow. Furthermore, the control actions can be very slow, depending on the equipment used for the offline measurements. In [75] a thermal process is also implemented with the detection principle based on ultrasound technology. In this case, a strict temperature control must be implemented for assuring the reliability of the method. Moreover, the process can be less efficient due to the flow divergence for the thermal process. The use of a resonant cavity sensor for the fat content determination is reported in [76], in which different methodologies are used to infer the fat percentage, including the cavity geometry, the operating frequency range and the magnitude and phase of reflection coefficient S_{11}. The author did not mention any automatic system for the standardization process.

In this thesis we propose an Automatic Standardization System based on resonant cavity sensor. In Fig. 4.14, a block diagram of this system conception with the main instruments is shown.

Figure 4.14: Block diagram of the Automatic Standardization System proposed.

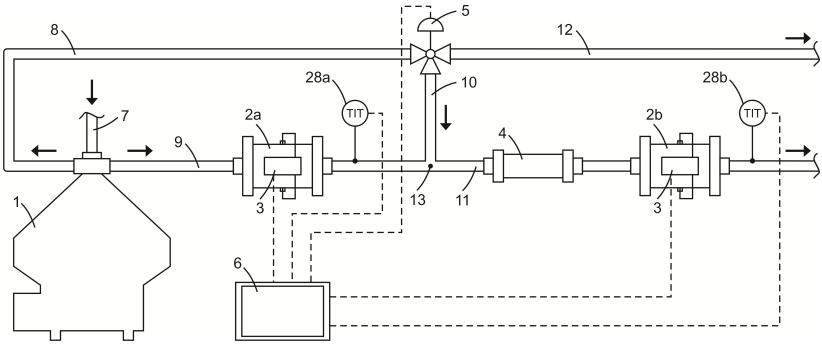

Source: The Author.

The system consists of two identical resonant cavity sensors (2a and 2b), a flow mixer (4), a three-way control valve (5), a centrifuge (1), temperature sensors (28a and 28b), and a control system (6). The working principle of the system is described as follows. The raw milk flow

enters in centrifuge 1 by means of pipe 7. The centrifuge separates the milk in two components: skimmed-milk and cream. There are different commercialized centrifuge models and the metrological parameters must be taken into account. After the separation process, cream stream flows to the control valve 5, which doses the amount of cream that returns, through pipe 10, to the skimmed-milk flow in pipe 9. The remaining amount of cream is sent to another process stage by means of pipe 12. The skimmed-milk stream flows to the intersection point 13, in which it is mixed with the cream flow from pipe 10. The standardized milk flows in pipe 11. The sensor 2a is mounted in the skimmed-milk flow 9, while the sensor 2b is mounted in the standardized milk flow 11, downstream the flow mixer 4, which is used for the mixture homogenization. The temperature sensors 28a and 28b are installed downstream the sensors 2a and 2b. The embedded RFTS circuits (3) are coupled to the sensors. The resonant frequency and magnitude of the transmission signal S_{21}, as well as the temperature values are processed in the control system 6 and properly converted to the actual fat content of the standardized milk. The sensor 2a acts as reference for the sensor 2b, providing more robustness to the system against variations in the total solids with no fat content, since the sensor 2a is mounted in the skimmed-milk flow, whose the fat content is minimum. The fat content variations due to the centrifuge 1 are corrected considering the magnitude and the resonant frequency parameters from both, 2a and 2b, sensors. The temperature sensors, 28a and 28b, allow an in-line calibration of the sensors 2a and 2b as the temperature flow changes, based on standards previously determined in the control system 6. The control valve 5 is the system actuator and controls the cream flow that returns to the skimmed-milk flow to standardize the milk to a desirable fat content.

4.2.5 Conclusions

The measurement system using a phase-locked resonant cavity sensor presented in this work may be effectively used for determining the concentration of total solids and/or fat constituents in milk. Measurements were performed using several samples from mixtures of different brands and types (whole, semi-skimmed and skimmed) of commercially available milks. The samples physicochemical constituents were obtained following AOAC methodology, verifying that they were in consonance with official regulation in Brazil. A high correlation and a linear dependence between the resonant frequency and the volume

fraction of total solids and fat were found (as stated in Table 4.4). Furthermore, the sensor's geometry was designed for compatibility with milking pipeline at industrial facilities. As a result, the complete system proves to be very attractive for in-line non-invasive and non-destructive monitoring of milk composition, providing a faster response and simpler installation compared to other reported techniques. Moreover, these encouraging results should allow us to explore other similar applications such as detection of milk adulteration used as raw material in derived dairy products. The experimental validation of this work is of great importance, once it provides the opportunity to overcome a latent problem in Brazilian dairy industry, the automation of the standardization process, one of the main stages of milk production. The proposed system explored in 4.2.4 is a detailed approach of an automatic standardization system, and it was designed after technical visits to three different milk production facilities in Paraná and Santa Catarina states in Brazil.

5 CONCLUSIONS

The overall contribution of this thesis is related to the exploration of measurement techniques based on a resonant cavity sensor, which was originally designed to be employed in industrial facilities for the in-line monitoring of different physical quantities.

The working principle of the sensor is intrinsic related to the effective permittivity of the material under test. As the permittivity changes the resonant frequency and magnitude of the transmission signal also change, allowing the indirect determination of a particular physical quantity.

The thesis comprises the electrical modeling and analysis of the sensor, as well as a semi-empirical modeling and analysis of a resonant frequency tracking system. By combining the resonant cavity sensor with a sophisticated measurement technique, we were able to investigate two industrial applications regarding the petroleum and dairy industries in Brazil.

The specific contributions of this work are addressed in the following section.

5.1 SPECIFIC CONTRIBUTIONS

5.1.0.1 The sensor's modeling and improvement

The previous characterization of the sensor demonstrated an impedance mismatching between the sensor's couplers and the external circuit, which is based on 50 Ω. Hence, in order to improve the measurement's reliability, an impedance matching analysis was performed. Two impedance matching networks, consisting of passive lumped elements, were implemented, enhancing the power transfer of the transmission signal and, as a consequence, the accuracy of the measurement system. Furthermore, a phenomenological mathematical model, based on an RLC resonant circuit, was developed. The sensor's dynamics were investigated using frequency and time domain tools. Two models, with and without the impedance matching networks, were simulated and experimentally validated using the sensor's S-parameters. The electric model, besides the permittivity variation of the material under test,

provide the whole description of the sensor's dynamics.

5.1.0.2 The resonant frequency tracking system

A semi-empirical modeling of a resonant frequency tracking system, employing the resonant cavity sensor, was developed. The measurement system is based on a phase-locked loop technique with a quadrature phase detector. One of the main advantage of this approach is that the resonant frequency information, as well as the magnitude information, can both be used to infer the measurement parameter, enhancing the robustness of the system. Furthermore, the resonant frequency is tracked without scanning all the RCS operational frequency range. The whole system dynamics, using an amplitude-phase transformation, was described under a rigorous mathematical perspective.

The system was considered in a general manner without any restriction on the system parameters, which enables the application of classic (linear and nonlinear) control tools to achieve the optimal performance. Exemplary, in this thesis a digital PI controller was used to guarantee the resonance tracking, where the control parameters were theoretically designed taking into account the linearized system. All the results were validated with real-life experiments. To do that, a dedicated RF circuit was implemented using off-the-shelf components.

The PLL based RFTS using an RCS is a legitimate contribution of this work, unpublished in the literature (as far the research permits confirm), providing a demonstration of the feasibility of this approach.

5.1.0.3 The industrial applications

Two industrial applications were investigated, where the first is the water fraction monitoring in a stratified water-gas flow. In this application, we verified that the system was capable of measuring in a full range (0% to 100%) with a mean water fraction sensitivity around $0.17\%/W_f$. The usage of a resonant cavity sensor as a water-cut meter proved to be feasible, but the strong dependence on the flow pattern may be a problem when there are distinct flow patterns at the same time. However, the combination of different technologies can be an attractive solution to overcome this flow regime dependence.

The second application regards the fat content monitoring in

bovine milk production. In this case, a high correlation and a linear dependence between the system response and the volume fraction of total solids and fat were found. We also assume that the encouraging results can allow us to explore other similar applications, such as detection of milk adulteration used as raw material in derived dairy products.

5.2 FUTURE WORKS

In view of suggestions for future works, the following topics can be addressed:

- Elaborate a nonlinear analysis of the PLL system, as a concern of experimentally determine the hold-in, pull-in and lock-in ranges;
- Analyze the implementation of new control strategies for the system response improvement;
- Implement an embedded resonant frequency tracking system with integrated circuits to enhance the system robustness and fidelity;
- Investigate new approaches using the RCS technology in combination with adjacent technologies, such as the electric capacitance tomography (ECT), in order to overcome the flow pattern dependence, and also to enhance the robustness of the measurement systems;
- Investigate a possible correlation between the milk constituents and both, magnitude and resonant frequency, information in order to enhance the measurement system feasibility.

5.3 PUBLICATIONS AND AWARDS

5.3.0.1 Publications as main author

- Ávila, H. E. L., Pagano, D. J., Sousa, F. R. (2015). Improving the performance of an RF resonant cavity water-cut meter using an impedance matching network. *Flow Measurement and Instrumentation*, 43:14-22. [19][1].

[1]DOI: 10.1016/j.flowmeasinst.2015.02.002, Copyright © 2015 Elsevier Ltd. - All rights reserved.

- Ávila, H. E. L. et. al. (2016). Determination of solids and fat contents in bovine milk using a phase-locked resonant cavity sensor. In *2016 1st International Symposium on Instrumentation Systems, Circuits and Transducers (INSCIT), pp. 1-4.* [16][2]

- Ávila, H. E. L., Sousa, F. R., Pagano, D. J. (2017). Resonant cavity water-cut meter with automatic resonance tracking system. In *2017 IEEE International Instrumentation and Measurement Technology Conference (I2MTC), pp. 1-6.* [44][3]

5.3.0.2 Publications as co-author

- Silva, M. J., Sousa, F. R., Santos, E. N. Pagano, D. J., Ávila H. E. L., Mota, F. R. M. Multiphase flow instrumentation and measurement research in Brazil. *IEEE Instrumentation & Measurement Magazine* , Vol. 20, Issue: 2, Apr. 2017. [77][4].

5.3.0.3 Awards

- Award certificates issued by the startup challenge "Ideas for Milk" organized by Brazilian Agricultural Research Corporation (*Empresa Brasileira de Pesquisa Agropecuária - EMBRAPA Gado de Leite*) in honor to the first place of the Local Finals in Porto Alegre and the third place of National Finals in Brasilia, for the recognition of the quality of the proposal entitled "*Sistema de monitoramento e controle em tempo real do percentual de gordura do leite para o processo de padronização*"[5].

[2]DOI: 10.1109/INSCIT.2016.7598207, Copyright © 2016 IEEE - All rights reserved.

[3]DOI: 10.1109/I2MTC.2017.7969669, Copyright © 2017 IEEE - All rights reserved.

[4]DOI: 10.1109/MIM.2017.7919136, Copyright © 2017 IEEE - All rights reserved.

[5]Local Finals: Porto Alegre, November 25th, 2016; National Finals: Brasilia, December 14th, 2016.

5.4 FINAL REMARKS

Considering the important position Brazil has in the world regarding the petroleum and milk production, we also can highlight that this thesis contributes to demonstrate the feasibility of employing a well established technology, combining a sophisticated measurement technique, for solving latent problems in the petroleum and dairy industries.

Moreover, in consideration of the verified lack in automatized process in most of the small and medium-sized dairy factories in Brazil, the experimental results of this research provided data for the proposal project of an automatic standardization system in a dairy facility for the in-line fat content monitoring. The proposal system comprises two resonant cavity sensors, besides instruments commonly used in industry in order to provide a more efficient and accurate standardization process. A brief comparison between the automatic system with the state of the art found in the literature is exposed, and as far the research permits confirm, this is the first project in literature for such system.

Appendices

A DETERMINATION OF THE STATE SPACE REPRESENTATION AND TRANSFER FUNCTION OF THE RCS ELECTRICAL MODEL FOR TIME DOMAIN AND FREQUENCY DOMAIN ANALYSIS

MISMATCHED CASE

From Fig. 2.16 (reproduced here in Fig. A.1), we deduce that the resonant circuit satisfies the following equations:

$$u_{rcs} - i_1 R_s - R_1(i_1 - i_L) = 0 \tag{A.1}$$

$$(i_L - i_1)R_1 + 2R_2 i_L + L\dot{i}_L + v_C + i_L R = 0 \tag{A.2}$$

where $R = R_1 R_s/(R_1 + R_s)$.

Solving for i_1 in (A.1), we have

$$i_1 = \tfrac{u_{rcs}}{R_1+R_s} + \tfrac{R_1}{R_1+R_s} i_L. \tag{A.3}$$

Substituting (A.3) in (A.2) and rearranging the equation, it follows that

$$L\dot{i}_L = (i_1 - i_L)R_1 - 2R_2 i_L - v_C - i_L R \tag{A.4}$$

$$\dot{i}_L = \frac{1}{L}\left[2(R_2 + R)i_L - v_C + \frac{R}{R_s}u_{rcs}\right].$$

Considering the inductor current $x_1 = i_L$ and the capacitor voltage $x_2 = v_c$ as states of the system, we can represent the state equations as follows:

$$\dot{x}_1 = \frac{1}{L}\left[2(R_2 + R)x_1 - x_2 + \frac{R}{R_s}u_{rcs}\right] \tag{A.5a}$$

$$\dot{x}_2 = \frac{x_1}{C}. \tag{A.5b}$$

The matrix representation in the form $\dot{\mathbf{x}} = \mathbf{A}\mathbf{x} + \mathbf{B}u(t)$, $y = \mathbf{C}\mathbf{x}$, considering $u(t) = u_{rcs}$ and $y(t) = y_{rcs}$ as the input and output of the system, respectively, is given by

Figure A.1: RCS's model for the first resonant mode, using a series RLC circuit.

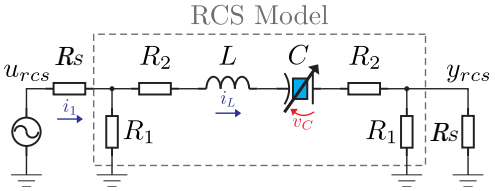

Source: The Author.

$$\begin{bmatrix} \dot{x}_1 \\ \dot{x}_2 \end{bmatrix} = \begin{bmatrix} 2(R_2+R)/L & -1/L \\ 1/C & 0 \end{bmatrix} \begin{bmatrix} x_1 \\ x_2 \end{bmatrix} + \begin{bmatrix} R/R_s \\ 0 \end{bmatrix} u_{rcs} \quad \text{(A.6)}$$

$$y_{rcs} = \begin{bmatrix} R & 0 \end{bmatrix} \begin{bmatrix} x_1 \\ x_2 \end{bmatrix}. \quad \text{(A.7)}$$

In frequency domain, we can use the forward transformation $G(s) = \mathbf{C}(s\mathbf{I} - \mathbf{A})^{-1}\mathbf{B} + \mathbf{D}$, to obtain the relation between the input U_{rcs} and the output Y_{rcs} of the system as follows

$$\frac{Y_{rcs}(s)}{U_{rcs}(s)} = \frac{\alpha s}{s^2 + 2\xi\omega_r s + \omega_r^2}, \quad \text{(A.8)}$$

where $\alpha = R^2/(R_s L)$ is a constant, $\omega_r = 1/\sqrt{LC}$ is the natural oscillation frequency, and $\xi = (R_2 + R)C/\sqrt{LC}$ is the damping coefficient.

MATCHED CASE

Analogously to the previous analysis, we can also derive the state equations for the matched case. From Fig. 2.18 (reproduced here in Fig. A.2), using the Kirchhoff's voltage law, we deduce that the four voltage loops exposed in the circuit can be represented as

$$u_{rcs} - i_1 R_s - v_{C_1} = 0, \quad \text{(A.9)}$$

$$v_{C_1} - L_1 \dot{i}_{L_1} - v_{C_2} - (i_{L_1} - i_L)R_1 = 0, \quad \text{(A.10)}$$

$$(i_{L_1} - i_L)R_1 - 2R_2 i_L - L\dot{i}_L - v_C - (i_L - i_{L_2})R_1 = 0, \quad \text{(A.11)}$$

$$(i_L - i_{L_2})R_1 - v_{C_3} - L_1 \dot{i}_{L_2} - v_{C_4} = 0. \quad \text{(A.12)}$$

Figure A.2: Series RLC model of the resonant cavity sensor including the impedance matching networks.

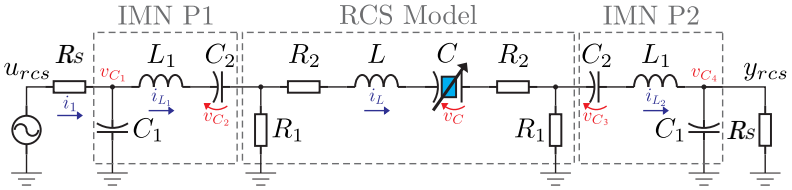

Source: The Author.

Additionally, using the Kirchhoff's current law, we have

$$i_1 - i_{L_1} - C_1 \dot{v}_{C_1} = 0, \tag{A.13}$$
$$i_{L_2} - C_1 \dot{v}_{C_4} - \frac{v_{C_4}}{R_s} = 0. \tag{A.14}$$

The loop currents can also be expressed as

$$i_1 = \frac{u_{rcs} - v_{C_1}}{R_s}, \tag{A.15}$$
$$i_L = C \dot{v}_C, \tag{A.16}$$
$$i_{L_1} = C_2 \dot{v}_{C_2}, \tag{A.17}$$
$$i_{L_2} = C_2 \dot{v}_{C_3}. \tag{A.18}$$

Substituting (A.15) in (A.9), and choosing the state variables that store energy in the circuit, in this case $x_1 = v_{C_1}$, $x_2 = i_{L_1}$, $x_3 = v_{C_2}$, $x_4 = i_L$, $x_5 = v_C$, $x_6 = i_{L_2}$, $x_7 = v_{C_3}$, $x_8 = v_{C_4}$, the equations (A.10)-(A.14) and (A.16)-(A.18) are them rearranged in order to obtain the following state equations:

$$
\begin{aligned}
\dot{x}_1 &= \frac{1}{C_1}\left[-\frac{x_1}{R_s} - x_2 + \frac{u_{rcs}}{R_s}\right] \\
\dot{x}_2 &= \frac{1}{L_1}\left[x_1 - R_1 x_2 - x_3 + R_1 x_4\right] \\
\dot{x}_3 &= \frac{x_2}{C_2} \\
\dot{x}_4 &= \frac{1}{L}\left[R_1 x_2 - 2(R_1 + R_2)x_4 - x_5 + R_1 x_6\right] \\
\dot{x}_5 &= \frac{x_4}{C} \\
\dot{x}_6 &= \frac{1}{L_1}\left[R_1 x_4 - R_1 x_6 - x_7 - x_8\right] \\
\dot{x}_7 &= \frac{x_6}{C_2} \\
\dot{x}_8 &= \frac{1}{C_1}\left[x_6 - \frac{x_8}{R_s}\right]
\end{aligned}
\tag{A.19}
$$

The matrix representation in the form $\dot{\mathbf{x}} = \mathbf{A}\mathbf{x} + \mathbf{B}u(t)$, $y = \mathbf{C}\mathbf{x}$, considering $u(t) = u_{rcs}$ and $y(t) = y_{rcs}$ as the input and output of the system, respectively, is given by

$$
\begin{bmatrix} \dot{x}_1 \\ \dot{x}_2 \\ \dot{x}_3 \\ \dot{x}_4 \\ \dot{x}_5 \\ \dot{x}_6 \\ \dot{x}_7 \\ \dot{x}_8 \end{bmatrix} =
\begin{bmatrix}
-\frac{1}{C_1 R_s} & -\frac{1}{C_1} & 0 & 0 & 0 & 0 & 0 & 0 \\
\frac{1}{L_1} & -\frac{R_1}{L_1} & -\frac{1}{L_1} & \frac{R_1}{L_1} & 0 & 0 & 0 & 0 \\
0 & \frac{1}{C_2} & 0 & 0 & 0 & 0 & 0 & 0 \\
0 & \frac{R_1}{L} & 0 & -\frac{2(R_1+R_2)}{L} & -\frac{1}{L} & \frac{R_1}{L} & 0 & 0 \\
0 & 0 & 0 & \frac{1}{C} & 0 & 0 & 0 & 0 \\
0 & 0 & 0 & \frac{R_1}{L_1} & 0 & -\frac{R_1}{L_1} & -\frac{1}{L_1} & -\frac{1}{L_1} \\
0 & 0 & 0 & 0 & 0 & \frac{1}{C_2} & 0 & 0 \\
0 & 0 & 0 & 0 & 0 & \frac{1}{C_1} & 0 & -\frac{1}{C_1 R_s}
\end{bmatrix}
\tag{A.20}
$$

$$
\begin{bmatrix} x_1 \\ x_2 \\ x_3 \\ x_4 \\ x_5 \\ x_6 \\ x_7 \\ x_8 \end{bmatrix} +
\begin{bmatrix} \frac{1}{R_s C_1} \\ 0 \\ 0 \\ 0 \\ 0 \\ 0 \\ 0 \\ 0 \end{bmatrix} u_{rcs}
$$

$$
y_{rcs} = \begin{bmatrix} 0 & 0 & 0 & 0 & 0 & 0 & 0 & 1 \end{bmatrix}
\begin{bmatrix} x_1 \\ x_2 \\ x_3 \\ x_4 \\ x_5 \\ x_6 \\ x_7 \\ x_8 \end{bmatrix}.
$$

Following the same procedure as in the mismatched case, we can use the forward transformation $G(s) = \mathbf{C}(s\mathbf{I} - \mathbf{A})^{-1}\mathbf{B} + \mathbf{D}$, to obtain the relation between the input U_{rcs} and the output Y_{rcs} of the system for frequency domain analysis as expressed in (A.21), where the coefficients of the characteristic equation are given in (A.22).

$$\frac{Y_{rcs}(s)}{U_{rcs}(s)} = \frac{CC_2^2R_1^2R_s s^3}{a_8s^8 + a_7s^7 + a_7s^7 + a_6s^6 + a_5s^5 + a_4s^4 + a_3s^3 + a_2s^2 + a_0}, \tag{A.21}$$

$$\begin{aligned}
a_8 &= CLC_1^2C_2^2L_1^2R_s^2 \qquad (A.22)\\
a_7 &= 2C[C_2^2(R_s^2C_1^2L_1(R_1L + R_1L + L_1(R_1 + R_2)) + LC_1L_1^2R_s)]\\
a_6 &= [C_1^2C_2^2(R_1^2C(L + 2L_1) + L_1(L_1 + 4CR_2R_1)) + 2CLL_1(C_1^2C_2\\
&\quad + C_1C_2^2)]R_s^2 + 4CC_1L_1(R_1(L_1 + L) + R_2L_1)R_s^2 + CLC_2^2L_1^2\\
a_5 &= [2C_1^2C_2^2R_1(L_1 + CR_2R_1) + 4CC_1C_2L_1(R_1(C_1 + C_2) + R_2(C_1 + C_2))\\
&\quad + 2CC_1C_2^2LR_1]R_s^2 + [C_2^2(C_1(R_1^2C(4L_1 + 2L) + 2L_1(L_1 + 4CR_2R_1))\\
&\quad + 2CLL_1) + 4CLC_1C_2L_1]R_s + 2CC_2^2L_1(R_1(L_1 + L) + R_2L_1)\\
a_4 &= [C_1^2(R_1(C_2^2R_1 + 2CC_2R_1 + 4CR_2C_2) + 2C_2L_1 + CL) + C_2^2(C(L\\
&\quad + R_1(4R_2C_1 + 2C_1R_1)) + 2C_1L_1) + 2CLC_1C_2]R_s^2 + [C_2^2(R_1(4C_1L_1\\
&\quad + 4CR_2C_1R_1 + 4CL_1 + 2CL) + 4CR_2L_1) + 4CC_1(C_2L_1(R_2 + R_1)\\
&\quad + LC_2R_1)]R_s + C_2^2(L_1(L_1 + 2CR_1(R_1 + 2R_2)) + CLR_1^2)\\
a_3 &= [2C_1^2(R_1(C_2 + CR_s) + CR_2R_s) + 2C_2^2(C_1R_1(R_1 + R_s)) + CR_1(R_1 + R_s)\\
&\quad + CR_2(2R_1 + R_s) + 2CLC_2]R_s + 2C_2^2R_1(L_1 + CR_2R_1) + 4CC_2L_1(R_1 + R_2)\\
&\quad + 2CLC_2(R_1 + R_s)\\
a_2 &= [C_1^2R_s + 2C_1C_2(2R_1 + R_2) + 4CC_1(R_1 + R_2) + C_2^2(2R_1 + R_s)\\
&\quad + 4CC_2(R_1 + R_2)]R_s + C_2[R_1(C_2^2 + 2C(R_1 + 2R_2)) + 2L_1] + CL\\
a_1 &= 2R_s(C_1 + C_2) + 2R_1(C + C_2) + 2R_2C\\
a_0 &= 1.
\end{aligned}$$

B NONLINEAR REPRESENTATION OF THE CLOSED LOOP DESCRIPTION USING A PID CONTROLLER

Consider the following PID control law:

$$y_c(t) = K_p\,\varphi_e(t) + K_i \int_0^t \varphi_e(\tau)d\tau + K_d \frac{d\varphi_e(t)}{dt}, \tag{B.1}$$

where K_p, K_i and K_d are the proportional, integral and derivative gains, respectively.

According to (3.22), and substituting (B.1) in (3.3), the first and second derivative of u_2 are expressed as

$$\dot{u}_2 = \omega_c + K_{vco}\left(K_p\,\varphi_e + K_i \int_0^t \varphi_e(\tau)\,d\tau + K_d \frac{d\varphi_e(t)}{dt}\right), \tag{B.2}$$

$$\ddot{u}_2 = K_{vco}(K_p\,\dot{\varphi}_e + K_i\,\varphi_e + K_d\ddot{\varphi}_e), \tag{B.3}$$

Knowing that $\varphi_e(t) = \phi_r - \varphi(t)$, and on account with (3.16), the first derivative of the phase error φ_e must consider that atan2 is a function of two variables and, as consequence, it has two partial derivatives. Hence, the first and second total differential are formulated as

$$\dot{\varphi}_e = \frac{y_{pdq}\dot{y}_{pdi} - y_{pdi}\dot{y}_{pdq}}{y_{pdq}^2 + y_{pdi}^2}. \tag{B.4}$$

$$\begin{aligned}\ddot{\varphi}_e = \frac{1}{(y_{pdq}^2 + y_{pdi}^2)^2}\Bigg[&(y_{pdq}^2 + y_{pdi}^2)(\ddot{y}_{pdq}y_{pdi} - y_{pdq}\ddot{y}_{pdi}) \\ &+2(y_{pdq}y_{pdi}(\dot{y}_{pdi}^2 - \dot{y}_{pdq}^2) + \dot{y}_{pdq}\dot{y}_{pdi}(y_{pdq}^2 - y_{pdi}^2))\Bigg].\end{aligned} \tag{B.5}$$

Rewriting (B.2)-(B.5) in terms of the variables (3.22) and inserting them into (3.27), we can describe the closed loop system by choosing two additional states

$$x_7 = \varphi_e, \quad x_8 = \int_0^t \varphi_e(\tau) d\tau. \tag{B.6}$$

Finally, the state space representation of the whole nonlinear system dynamics is described as

$$\begin{aligned}
\dot{x}_1 &= x_3 \\
\dot{x}_2 &= x_4 \\
\dot{x}_3 &= u_1 \cos x_2 - 2\xi\omega_r x_3 + x_1((\dot{u}_2 + x_4)^2 - \omega_r^2) \\
\dot{x}_4 &= -\frac{u_1}{x_1}\sin x_2 - 2\left(\xi\omega_r + \frac{x_3}{x_1}\right)(\dot{u}_2 + x_4) - \ddot{u}_2 \\
\dot{x}_5 &= \omega_g[K_{pdq}\, x_1(-x_2 - \Delta\phi_{rcs} + \Delta\phi_q) - x_5] \\
\dot{x}_6 &= \omega_g[K_{pdi}\, x_1(x_2 + \Delta\phi_{rcs} - \Delta\phi_i + \pi/2) - x_6] \\
\dot{x}_7 &= \frac{\omega_g x_1}{x_5^2 + x_6^2}\Big[K_{pdi}(x_2 + \Delta\phi_{rcs} - \Delta\phi_i + \pi/2)\, x_5 - K_{pdq}(-x_2 \\
&\quad -\Delta\phi_{rcs} + \Delta\phi_q)\, x_6\Big] \\
\dot{x}_8 &= \phi_r - \text{atan2}(x_5, x_6),
\end{aligned} \tag{B.7}$$

where $\dot{u}_2$ and $\ddot{u}_2$ are expressed, respectively as

$$\dot{u}_2 = \omega_c + K_{vco}(K_p x_7 + K_i x_8 + K_d \dot{x}_7), \tag{B.8}$$

$$\ddot{u}_2 = K_{vco}(K_p \dot{x}_7 + K_i x_7 + K_d \ddot{x}_7). \tag{B.9}$$

As stated in (B.5), the second derivative of x_7 is given by

$$\ddot{x}_7 = \frac{(x_5^2 + y_6^2)(\ddot{x}_5 x_6 - x_5 \ddot{x}_6) + 2(x_5 x_6(\dot{x}_6^2 - \dot{x}_5^2) + \dot{x}_5 \dot{x}_6(x_5^2 - x_6^2))}{(x_5^2 + x_6^2)^2}, \tag{B.10}$$

where the second derivatives of x_5 and x_6, are respectively expressed as

$$\ddot{x}_5 = \omega_g[(-x_2 - \Delta\phi_{rcs} + \Delta\phi_q)(K_{pdq}(x_3 - x_1\omega_g)) - K_{pdq} x_1 x_4 + \omega_g x_5], \tag{B.11}$$

$$\ddot{x}_6 = \omega_g[(x_2 + \Delta\phi_{rcs} - \Delta\phi_i + \pi/2)(K_{pdi}(x_3 - x_1\omega_g)) - K_{pdi} x_1 x_4 + \omega_g x_6]. \tag{B.12}$$

If we substitute (B.11)and (B.12) in (B.10), we can verify that the first and second derivative of u_2 are formed only by the states of $\mathbf{x}$, and as a consequence (B.7) can also be considered as a nonlinear and autonomous system in the form $\dot{\mathbf{x}} = \mathbf{F}(\mathbf{x}) + \mathbf{G}(\mathbf{u})$.

BIBLIOGRAPHY

[1] E. Nyfors and P. Vainikainen. *Industrial Microwave Sensors*. Artech House, Norwood, MA, 1989.

[2] Ming Huang et al. RF sensor for online determination of granular dielectric materials weight. In *Information and Automation, 2008. ICIA 2008. International Conference on*, pages 1792–1796, June 2008.

[3] D. J. Thomson et al. RF cavity passive wireless sensors with time-domain gating-based interrogation for SHM of civil structures. *IEEE Sensors J.*, 9(11):1430–1438, Nov 2009.

[4] V. Etxebarria et al. Very high sensitivity displacement sensor based on resonant cavities. *IEEE Sensors J.*, 10(8):1335–1336, Aug 2010.

[5] Christine Barthod et al. Resonant force sensor using a PLL electronic. *Sensors and Actuators A: Physical*, 104(2):143–150, 2003.

[6] Soon-Young Hong et al. Wireless temperature measurement system with rf transceiver and powerless sensor. In *Power Electronics and ECCE Asia (ICPE-ECCE Asia), 2015 9th International Conference on*, pages 2602–2607, June 2015.

[7] B. Milovanovic et al. A simple method for permittivity measurement using microwave resonant cavity. In *Microwaves and Radar, 1998. MIKON '98., 12th International Conference on*, volume 3, pages 705–709 vol.3, May 1998.

[8] O. Cakmak et al. Precision density and viscosity measurement using two cantilevers with different widths. *Sensors and Actuators A: Physical*, 232:141 – 147, 2015.

[9] Benjamin A. Bircher et al. Automated high-throughput viscosity and density sensor using nanomechanical resonators. *Sensors and Actuators B: Chemical*, 223:784 – 790, 2016.

[10] Sandeep Kumar Vashist. A review of microcantilevers for sensing applications, June 2007. [Online; posted 18-June-2007].

[11] Byung Su Chang et al. Automatic mode matching control loop design and its application to the mode matched mems gyroscope. In *Vehicular Electronics and Safety, 2007. ICVES. IEEE International Conference on*, pages 1–6, Dec 2007.

[12] S R Wylie et al. RF sensor for multiphase flow measurement through an oil pipeline. In *Measurement Science and Technology*, volume 17, pages 2141–2149, 2006.

[13] E. Scussiato. Medidor de fração de água para escoamento bifásico (água e óleo) utilizando técnicas de microondas e cavidades ressonantes. Master's thesis, Universidade Federal de Santa Catarina, Florianópolis, Brasil, 2010.

[14] H. E. L. Ávila. Análise e caracterização de um sensor eletromagnético de cavidade ressonante aplicado à medição de fração de água em uma mistura bifásica. Master's thesis, Universidade Federal de Santa Catarina, UFSC, Florianópolis, SC, Brasil, 2013.

[15] Ebbe Gustaf Nyfors. Cylindrical microwave resonator sensors for measuring materials under flow. Master's thesis, UHelsinki University of Technology, Finland, 2000.

[16] H. E. L. Ávila, R. R. Antayhua, S. Verrruck, G. R. Liz, L. C. Pereira, E. S. Prudencio, F. R. Sousa, and D. J. Pagano. Determination of solids and fat contents in bovine milk using a phase-locked resonant cavity sensor. In *2016 1st International Symposium on Instrumentation Systems, Circuits and Transducers (INSCIT)*, pages 1–4, Aug 2016.

[17] International, May 2018. [online] `https://www.eia.gov/beta/international/`.

[18] Top milk producing countries in the world, May 2018. [online] `https://www.worldatlas.com/articles/top-cows-milk-producing-countries-in-the-world.html`.

[19] H. E. L. Ávila et al. Improving the performance of an RF resonant cavity water-cut meter using an impedance matching network. *Flow Measurement and Instrumentation*, 43:14–22, 2015.

[20] J. C. Maxwell. A dynamical theory of the electromagnetic field. *Philosophical Transactions of the Royal Society of London*, 155:459 – 512, 1865.

[21] David M. Pozar. *Microwave Engineering.* John Wiley & Sons, Inc., Danver, MA, 2005.

[22] W. J. Ellison et al. Water: a dielectric reference. *Journal of Molecular Liquids*, 68(2–3):171–279, 1996.

[23] Devendra K. Misra. *Radio-Frequency and Microwave Communication Circuits: Analysis and Design.* John Wiley & Sons, Hoboken, New Jersey, 2004.

[24] V. Iyer, S.N. Makarov, D.D. Harty, F. Nekoogar, and R. Ludwig. A lumped circuit for wideband impedance matching of a non-resonant, short dipole or monopole antenna. In *IEEE Transactions on Antennas and Propagation*, volume 58, 2010.

[25] T. Yabuhara, K. Kato, K. Tsuchiya, T. Shigihara, T. Uzuka, and H. Takahashi. Development of the re-entrant type resonant cavity applicator for brain tumor hyperthermia - experimental heating results. In *Engineering in Medicine and Biology Society, 2006. EMBS '06. 28th Annual International Conference of the IEEE*, 2006.

[26] Sanghoon Cheon, Yong-Hae Kim, Seung-Youl Kang, Myung-Lae Lee, Jong-Moo Lee, and Taehyoung Zyung. Circuit-model-based analysis of a wireless energy-transfer system via coupled magnetic resonances. In *IEEE Transactions on Industrial Electronics*, volume 58, 2011.

[27] Hee-Seung Kim, Do-Hyun Won, and Byung-Jun Jang. Simple design method of wireless power transfer system using 13.56 mhz loop antennas. In *IEEE International Symposium on Industrial Electronics (ISIE)*, 2010.

[28] Christopher Bowick. *Electromagnetic mixing formulas and applications.* RF Circuit Design, Burlington, USA, 2008.

[29] G. Gonzalez. *Microwave Transistor Amplifiers: Analysis and Design.* Prentice Hall, New Jersey, 1997.

[30] S Al-Hajeri et al. Real time EM waves monitoring system for oil industry three phase flow measurement. In *Journal of Physics: Conference Series*, volume 178, pages 1–6, 2009.

[31] H. S. Wasisto et al. Handheld micromechanical cantilever mass sensor for early detection of carbon nanoparticles. In *Sensors and*

Measuring Systems 2014; 17. ITG/GMA Symposium; Proceedings of, pages 1–6, June 2014.

[32] C. Kharrat et al. H∞ loop-shaping control of a pll-based oscillation loop for dynamic resonance tracking in nems mass sensors arrays. In *Control Conference (ECC), 2009 European*, pages 4997–5002, Aug 2009.

[33] H. Sohanian-Haghighi and A. Davaie-Markazi. Resonance tracking of nonlinear mems resonators. *Mechatronics, IEEE/ASME Transactions on*, 17(4):617–621, Aug 2012.

[34] A. Kumar et al. A frequency scan scheme for pll-based locking to high-q mems resonators. In *VLSI Design (VLSID), 2015 28th International Conference on*, pages 71–74, Jan 2015.

[35] Yunseog Hong et al. Noncontact proximity vital sign sensor based on pll for sensitivity enhancement. *IEEE Trans. Biomed. Circuits Syst.*, 8(4):584–593, Aug 2014.

[36] S. Kim et al. Heart rate detection during sleep using a flexible RF resonator and injection-locked pll sensor. *IEEE Rev. Biomed. Eng*, 62(11):2568–2575, 2015.

[37] D.W. Clarke and T. Ghaoud. A dual phase-locked loop for vortex flow metering. *Flow Measurement and Instrumentation*, 14(1–2):1 – 11, 2003.

[38] M. Aiello et al. Synchronization techniques for power quality instruments. *IEEE Trans. Instrum. Meas.*, 56(5):1511–1519, Oct 2007.

[39] A. Cataliotti et al. A phase-locked loop for the synchronization of power quality instruments in the presence of stationary and transient disturbances. *IEEE Trans. Instrum. Meas.*, 56(6):2232–2239, Dec 2007.

[40] Rolando E. Best. *Phae-locked loops, desighn, simulation, and applications*. McGraw-Hill, Oxford, UK, 2009.

[41] atan2. `https://en.wikipedia.org/wiki/Atan2`. Accessed: 2018-07-19.

[42] T. Brack et al. Dynamics and stability of phase controlled oscillators. *J. Dyn. Sys.*, 138:071007–071007–12, 2016.

[43] K. J. Astrom and B. Wittenmark. *Computer Controlled Systems*. Prentice Hall, Upper Saddle River, NJ, 1984.

[44] H. E. L. Ávila, F. R. Sousa, and D. J. Pagano. Resonant cavity water cut meter with automatic resonance tracking system. In *2017 IEEE International Instrumentation and Measurement Technology Conference (I2MTC)*, pages 1–6, May 2017.

[45] Gioia Falcone, Geoffrey F. Hewitt, and Claudio Alimonti. *Multiphase Flow Metering: Principles and Applications*. Elsevier, Oxford, UK, 2009.

[46] Yemada Taitel and A. E. Dukler. A model for predicting flow regime transitions in horizontal and near horizontal gas-liquid flow. *AIChE Journal*, 22(1):47–55, 1976.

[47] M. E. Charles, G. W. Govier, and G. W. Hodgson. The horizontal pipeline flow of equal density oil-water mixtures. *The Canadian Journal of Chemical Engineering*, 39(1):27–36, 1961.

[48] J. L. Trallero, C. Sarica, and J. P. Brill. A study of oil-water flow patterns in horizontal pipes. *Society of Petroleum Engineers*, 12(3):165–172, 1997.

[49] O.M.H. Rodriguez and R.V.A. Oliemans. Experimental study on oil–water flow in horizontal and slightly inclined pipes. *International Journal of Multiphase Flow*, 32(3):323 – 343, 2006.

[50] Luai M. Al-Hadhrami, S. M. Shaahid, Lukman O. Tunde, and A. Al-Sarkhi. Experimental study on the flow regimes and pressure gradients of air-oil-water three-phase flow in horizontal pipes. *The Scientific World Journal*, 2014:1 – 11, 2014.

[51] H. E. L. Ávila et al. Water fraction measurement using a RF resonant cavity sensor. In *19th IMEKO TC-4 Symposium Measurements of Electrical Quantities*, pages 281–285, Barcelona, Spain, July 2013.

[52] Benoît Lamarche et al. Does milk consumption contribute to cardiometabolic health and overall diet quality? *Canadian Journal of Cardiology*, pages 1–7, 2016.

[53] Ellen Muehlhoff, Anthony Bennett, and Deirdre McMahon, editors. *Milk and dairy products in human nutrition*. Food and Agriculture Organization of the United Nations, Rome, 2013.

[54] Stefano Gerosa and Jakob Skoet. Milk availability: trends in production and demand and medium-term outlook. *Food and Agriculture Organization of the United Nations*, (12-01):1–38, 2012. Special issue on bio-robotics.

[55] Milk production, Apr 2016. [online] `http://www.fao.org/agriculture/dairy-gateway/milk-production/en/#.Vx58wTArKUk`.

[56] Michael Griffin. Food outlook: Milk and milk products. Technical report, Food and Agriculture Organization of the United Nations, November 2013.

[57] Renata Bongiolo Magenis et al. Rheological, physicochemical and authenticity assessment of minas frescal cheese. *Food Control*, 45:22–28, 2014.

[58] P. Walstra et al. *Dairy Science and Technology*. Food science and technology 146. CRC/Taylor and Francis, New York, second edition, 2006.

[59] Dechen Liu, , et al. A green technology for the preparation of high capacitance rice husk-based activated carbon. *Journal of Cleaner Production*, 112, Part 1:1190–1198, 2016.

[60] G. Durante et al. Electrical impedance sensor for real-time detection of bovine milk adulteration. *IEEE Sensors J.*, 16(4):861–865, 2016.

[61] L. d. S. Ribeiro et al. Development of a hardware platform for detection of milk adulteration based on near-infrared diffuse reflection. *IEEE Trans. Instrum. Meas.*, PP(99):1–9, 2016.

[62] P. S. Venkateswaran et al. Rapid and automated measurement of milk adulteration using a 3D printed optofluidic microviscometer OMV. *IEEE Sensors J.*, 16(9):3000–3007, 2016.

[63] Daniel Agranovich et al. A microwave sensor for the characterization of bovine milk. *Food Control*, 63:195–200, 2016.

[64] K. H. Joshi et al. Online monitoring of milk quality using electromagnetic wave sensors. In *2015 9th International Conference on Sensing Technology (ICST)*, pages 700–705, Auckland, New Zealand, Dec 2015.

[65] Masataka Kawasaki et al. Near-infrared spectroscopic sensing system for on-line milk quality assessment in a milking robot. *Computers and Electronics in Agriculture*, 63(1):22–27, 2008. Special issue on bio-robotics.

[66] Departamento Intersindical de Estatística e Estudos Socioeconômicos DIEESE. Anuário do trabalho na micro e pequena empresa. Technical report, Serviço Brasileiro de Apoio às Micro e Pequenas Empresas - SEBRAE, 2013.

[67] William Horwitz and George W. Latimer Jr., editors. *Official methods of analysis of AOAC International.* AOAC - Association of Analytical Chemistry, Washington, 18th edition, 2005.

[68] Diário Oficial da União, editor. *Ministério da Agricultura. Secretaria de Defesa Agropecuária. Regulamento técnico de produção, identidade e qualidade do leite tipo A, cru refrigerado e de leite pasteurizado. Instrução Normativa 62*, Brasília, 2012.

[69] Pallavi R. Malame et al. Microwave reflectometry based electrical characterization of milk for adulteration detection. *Advance in Electronic and Electric Engineering*, 4(5):487–492, 2014.

[70] Dale A. Seiberling. Continuous separating and standardizing of milk, 03 1976. [online] `https://patents.google.com/patent/US3946113`.

[71] Tibor Pato. Method and apparatus for regulating the fat content of milk, 02 1978. [online] `https://patents.google.com/patent/US4075355A/en?oq=US4075355`.

[72] Karl-Heinz Zettier. Process and system for regulating the fat content of milk and cream, 01 1997. [online] `https://patents.google.com/patent/US5591469A/en?oq=US5591469`.

[73] Joseph H. Lester. Process for standardizing milk by monitoring the fat content of the blended milk product, 04 1977. [online] `https://patents.google.com/patent/US4017643A/en?oq=US4017643`.

[74] Michael G. O'Keefe and Richard Oberrieth. Apparatus for continuously controlling butterfat content of reconstituted milk, 03 1979. [online] `https://patents.google.com/patent/US4144804A/en?oq=US4144804`.

[75] William C. Winder and Richard J. Wagner. Method and apparatus for controlling composition of milk, 03 1979. [online] https://patents.google.com/patent/US4145450A/en?oq=US4145450.

[76] Michael O. Fryer, Andrea J. Hills, and John L. Morrison. Method and apparatus for measuring butterfat and protein content using microwave absorption techniques, 11 2000. [online] https://patents.google.com/patent/US6147502A/en?oq=US6147502.

[77] M. J. Da Silva, F. R. De Sousa, E. N. Dos Santos, D. J. Pagano, H. E. De Lima Ávila, and F. R. M. Da Mota. Multiphase flow instrumentation and measurement research in brazil. *IEEE Instrumentation Measurement Magazine*, 20(2):57–62, 2017.